Eur. Phys. J. A **27**, 269–285 (2006)
DOI 10.1140/epja/i2005-10268-x

THE EUROPEAN PHYSICAL JOURNAL A

# Resonances and final-state interactions in the reaction pp → pK$^+$Λ

A. Sibirtsev[1], J. Haidenbauer[2,a], H.-W. Hammer[1], and S. Krewald[2]

[1] Helmholtz-Institut für Strahlen- und Kernphysik (Theorie), Universität Bonn, Nußallee 14-16, D-53115 Bonn, Germany
[2] Institut für Kernphysik (Theorie), Forschungszentrum Jülich, D-52425 Jülich, Germany

Received: 19 December 2005 / Revised version: 13 February 2006 /
Published online: 4 April 2006 – 
Communicated by V. Vento

**Abstract.** A study of the strangeness production reaction $pp \to pK^+\Lambda$ for excess energies of $\epsilon \leq 150\,\mathrm{MeV}$, accessible at high-luminosity accelerator facilities like COSY, is presented. Methods to analyze the Dalitz plot distribution and angular spectra in the Jackson and helicity frames are worked out and suitable observables for extracting information on low-lying resonances that couple to the $K\Lambda$ system and for determining the $\Lambda p$ effective-range parameters from the final-state interaction are identified and discussed. Furthermore, the chances for identifying the reaction mechanism of strangeness production are investigated.

**PACS.** 13.75.Ev Hyperon-nucleon interactions – 13.75.Jz Kaon-baryon interactions – 14.20.Gk Baryon resonances with $S = 0$ – 25.40.Ny Resonance reactions

## 1 Introduction

Strangeness production reactions like $pp \to pK^+\Lambda$ are interesting for various reasons. First of all such reactions require the creation of a new quark flavour which can occur out of the vacuum but also from the quark-antiquark sea in the protons. Thus, a thorough and dedicated study of the strangeness production mechanism in those reactions has the potential to ultimately deepen our understanding of the internal structure of the baryons. Furthermore, there are indications that several excited states of the nucleon decay into the $\Lambda K$ channel. However, reliable and quantitative information is rather sparse. Investigations of $pp \to pK^+\Lambda$ might allow to significantly improve the available data base. This concerns specifically the $S_{11}(1650)$ and $P_{11}(1710)$ resonances. Finally, the presence of protons as well as $\Lambda$ hyperons in the final state opens the possibility to study the interaction between those baryons, which is still poorly known but whose knowledge is essential for questions related to the validity of the $SU(3)$ flavour symmetry.

Concerning the mechanism of strangeness production in nucleon-nucleon ($NN$) collisions one has to concede that it is not yet understood —although there is a significant experimental data base and despite of numerous dedicated theoretical investigations. Until recently only data at fairly high energies were available. The analysis [1–6] of those data indicated that different production mechanisms are compatible with the experimental evidence. The data on the $pp \to pK^+\Lambda$ reaction cross-section and also the momentum spectra of the final $K$-meson and $\Lambda$-hyperon can be well reproduced either by $K$-meson or $\pi$-meson exchange models. Only the large amount of $\Lambda$-hyperon recoil polarization data [7–10] collected at high energies from the inclusive $pp \to \Lambda X$ reaction can be considered as evidence for a $\pi$-meson exchange dominance [11–14].

At high energies where the Regge phenomenology is applicable the energy dependence of the reaction cross-section should indicate the reaction mechanism. But one has to keep in mind that at those energies the energy dependence of the $K$-meson and $\pi$-meson exchange is almost identical. Indeed, in Regge theory the energy dependence of the reaction amplitude is governed by the exchange trajectory $\alpha(t)$ via $s^{\alpha(t)}$, where $s$ is the square of the invariant collision energy and $t$ is the squared four-momentum transferred from the initial nucleon to the final nucleon or hyperon, for the exchange of a nonstrange as well as of a strange meson. The overall data analysis indicates that the pion exchange trajectory amounts to $\alpha_\pi(t) = 0.85(t - m_\pi^2)$, while the kaon exchange is given by $\alpha_K(t) = 0.7(t - m_K^2)$. Within the Regge theory the difference between the $\pi$ and $K$ trajectories is only due to the mass of the exchange particles and not by the trajectory intercept at $t = 0$. On the other hand, one can certainly say that the data exclude a dominance of the $\rho$-meson exchange, whose trajectory is given by $\alpha_\rho(t) = 0.5 + 0.9t$. The $K^*$ and $K^{**}$ exchanges have also large intercepts, 0.5 and 0.35, respectively, and

[a] e-mail: j.haidenbauer@fz-juelich.de

are likewise not supported by the available data for the $pp \to pK^+\Lambda$ reaction cross-section.

Over the last few years the COSY facility has provided a large amount of accurate experimental data on strangeness production in $NN$ collisions at low energies [15–23]. Theoretical model studies [24–30] that dealt with those data suggested that the excitation of resonances in the $K\Lambda$ channel could play an important if not dominant role for the reaction $pp \to pK^+\Lambda$ in the near-treshold regime. If this is indeed the case one has to be cautious in extrapolating from the mechanisms that dominate at high energies, *i.e.* exchanges by different meson trajectories, to what happens at low energies. Specifically, it cannot be excluded that, say, vector mesons like $\rho$ couple strongly to the resonances in question, namely the $S_{11}(1650)$ and the $P_{11}(1710)$, and therefore play a decisive role in the strangeness production near threshold. Also, the investigations so far have made clear that the interaction between the particles in the final state plays a role and influences significantly the energy dependence of the production cross-section in the threshold region. Among the three possible channels ($K\Lambda$, $KN$, $\Lambda N$) it is presumably only the final-state interaction (FSI) in the $\Lambda N$ system which is important [31–36]. The corresponding scattering lengths are not well determined from the few $\Lambda N$ (and $\Sigma N$) scattering data that exist, but are expected to be in the order of 1 to 2 fm [37–40].

In this paper we present a study of the strangeness production reaction $pp \to pK^+\Lambda$ in the energy range accessible at the COSY accelerator facility, *i.e.* for excess energies up to $\epsilon \approx 150\,\mathrm{MeV}$. However, it is not the aim of our work to suggest yet another model for that reaction. Rather we want to embark on a more general analysis of this reaction. In view of the complexity of the situation where neither the production mechanism nor the final-state interaction are reliably known we restrict ourselves to the case of unpolarized experiments. Also, we consider only two reaction mechanisms, namely pion exchange and $K$-meson exchange. However, we want to emphasize that these mechanisms are understood as being representatives of a whole class of reaction scenarios rather than of the concrete processes. Accordingly, $K$ exchange represents a scenario where there is strangeness exchange in the production mechanism and where the elementary reaction amplitude ($KN \to KN$) is governed by $t$-channel exchange diagrams, so that its energy dependence is rather smooth. In particular, there are no resonances involved. Pion exchange, on the other hand, stands for a scenario where no strangeness exchange occurs in the production mechanism. At the same time the elementary reaction amplitude ($\pi N \to K\Lambda$) is dominated by resonance excitations ($S_{11}(1650)$, $P_{11}(1710)$, $P_{13}(1720)$, ...) which implies a strong and characteristic energy dependence. In our investigation we will look at the consequences of these two classes of reaction scenarios for the reaction $pp \to pK^+\Lambda$ and analyse their signature in observables like the total cross-section, angular distributions and the Dalitz plot. Thereby we will address the following questions: a) Is it possible to discriminate between different production mechanisms? b) What can be learned about the FSI? Is it possible to extract the effective-range parameters for the $\Lambda p$ interaction? c) Can one determine the parameters of the $S_{11}(1650)$- and the $P_{11}(1710)$-resonance from the strangeness production reaction?

There are, of course, additional important and more concrete questions. For example, is the strangeness-exchange mechanism dominated by the $KN \to KN$ reaction or rather by $K^*N \to KN$? Likewise, are the resonances predominantly excited by pion exchange or is $\rho$ exchange important as well? Those questions will not and cannot be addressed in the present investigation. For that a throrough investigation of the spin dependence of the various observables is required which is beyond the scope of the present paper.

Our paper is organized as follows: in sect. 2 we introduce those experimental observables which can be used as a tool for investigating the properties of the $\Lambda p$ final-state interaction and of resonances in the $K\Lambda$ channel but also for a possible identification of the reaction dynamics. Section 3 provides the overall structure of the reaction amplitude and describes the explicit application to the $\pi$- and $K$-meson exchange mechanisms. The $KN \to KN$ and $\pi N \to K\Lambda$ transition amplitudes and a description of the treatment of the $\Lambda p$ final-state interaction are given in sects. 4, 5 and 6, respectively. The total $pp \to pK^+\Lambda$ reaction cross-section is analyzed in sect. 7, while sects. 8 and 9 focus on the Dalitz plot and on angular correlations. The paper ends with a summary of our results and some concluding remarks.

## 2 Kinematic constraints and relevant observables

In this section we provide a detailed discussion of those observables that are directly related to the issues we want to address (FSI effects, resonance parameters, production mechanism). Some of these observables like Dalitz plot distributions or invariant mass spectra are well known and widely used in the analysis of experiments. Other observables discussed below can be determined only through the full exclusive reconstruction of the reaction events, which can be done only at a some specific experimental facilities like COSY. Since the formalism can be applied to any three-body final-state reaction we discuss it in a more general form. Generally speaking the formalism can be applied to the analysis of any meson production in $NN$ collisions ($\pi$, $\eta$, $\omega$, ...), independently of the collision energy.

For the consideration of different kinematical variables it is convenient to express the invariant amplitude for the reaction $a + b \to 1 + 2 + 3$, as depicted in fig. 1d), in terms of one initial and four final independent invariants, namely by

$$s = (P_a + P_b)^2\,,$$
$$s_1 = (P_1 + P_2)^2\,,$$
$$s_2 = (P_2 + P_3)^2\,,$$

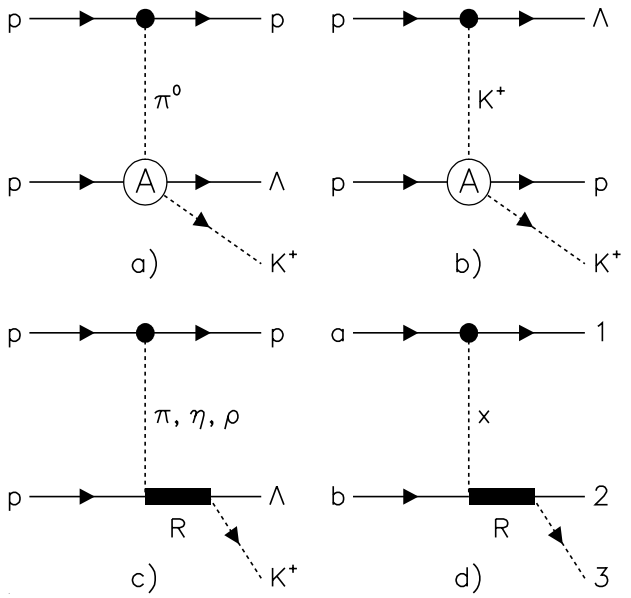


**Fig. 1.** a) Pion and b) kaon exchange contributions to the reaction $pp \to pK^+\Lambda$, included in our investigation. $A$ denotes the full ($KN$ or $\pi N \to K^+\Lambda$) transition amplitudes. c) Representation of the resonance model for the reaction $pp \to pK^+\Lambda$. d) General diagram for $t$-channel contributions to the reaction $a + b \to 1 + 2 + 3$ with intermediate resonances $R$ coupled to the $\{23\}$ subsystem and exchange particle $x$.

$$t_1 = (P_a - P_1)^2\,,$$
$$t_2 = (P_b - P_3)^2\,, \tag{1}$$

where the $P_i$ denote the four-momentum of the corresponding particle $i$. The fifth independent final variable is the azimuthal rotation angle $\phi$ around the beam axis. We also use the excess energy $\epsilon = \sqrt{s} - m_1 - m_2 - m_3$. The differential reaction cross-section can then be written as a function of the four invariants at fixed $s$,

$$\frac{\mathrm{d}\sigma}{\mathrm{d}s_1\mathrm{d}s_2\mathrm{d}t_1\mathrm{d}t_2} = \frac{|\mathcal{M}(s,s_1,s_2,t_1,t_2)|^2}{2^{10}\pi^4\lambda(s,m_a^2,m_b^2)\sqrt{-\Delta_4}}\,, \tag{2}$$

where the $\phi$-dependence is already integrated out. Here $\lambda(x,y,z) = (x-y-z)^2 - 4yz$ is the Källen function and $\Delta_4$ is the Gramm determinant of a $4 \times 4$ symmetric matrix whose elements are a combination of $s$, $s_1$, $s_2$, $t_1$, $t_2$ and of the masses of the initial and final particles [41]. The physical region of the invariants is determined by the condition $\Delta_4 \leq 0$. The integration of eq. (2) over $t_1$ and $t_2$ results in the famous Dalitz plot [42]

$$\frac{\mathrm{d}\sigma}{\mathrm{d}s_1\mathrm{d}s_2} = \frac{|\mathcal{M}(s,s_1,s_2)|^2}{2^8\pi^3 s\lambda^{1/2}(s,m_a^2,m_b^2)}\,. \tag{3}$$

If the reaction amplitude is constant, *i.e.* $\mathcal{M} = \mathrm{const}$, then the distribution of the Dalitz plot is isotropic. Therefore, any resonance or FSI can be detected through a Dalitz plot analysis. However, possible structures in the subsystem formed by particles 1 and 2 (we use the shorthand notation $\{12\}$ etc. in the following), say, can interfere with those appearing in the $\{23\}$ subsystem because the differential cross-section is a function of both invariants $s_1$ and $s_2$, and this dependence does not factorize. Such interferences might produce so-called kinematic reflections in the Dalitz plot projections, *i.e.* in the invariant mass spectra. In case of the reaction $pp \to pK^+\Lambda$ the Dalitz distribution is a useful tool to study resonances in the $K^+\Lambda$ system and also the $\Lambda p$ (final state) interaction.

Obviously, the Dalitz plot presents already partially integrated data, while the full information about the reaction dynamics for an unpolarized 3-body final state is given explicitly by eq. (2). Different specific and more practical variables were proposed by Gottfried and Jackson considering the $\{23\} \to 2 + 3$ decay and possible resonances coupled to the $\{23\}$ subsystem [43,44]. Furthermore, for a more general case it is interesting to investigate the relation between the production mechanism and the angular correlations in the decay of the unstable intermediate particle. In that case it is more useful to consider the decay $\{23\} \to 2 + 3$ and to measure the angular distribution of particle 3 in the rest frame of $\{23\}$.

In order to understand the meaning of the angular correlations one best considers the reaction $a + b \to 1 + 2 + 3$ in terms of the subprocess $a + b \to 1 + \{23\}$ and the subsequent $\{23\} \to 2 + 3$ decay, as depicted in fig. 1d). In that case the 3-body phase space can be expressed in terms of the $2\times2$-body phase space convolution as

$$\mathrm{d}\Phi_3 = \mathrm{d}\Phi_2(s, m_1^2, s_2)\,\mathrm{d}\Phi_2(s_2, m_2^2, m_3^2)\,\mathrm{d}s_2, \tag{4}$$

where the 2-body phase space, $\Phi_2$, might be taken in different representations. In particular, it is convenient to use

$$\mathrm{d}\Phi_2(s, m_1^2, s_2) = \frac{\pi}{2\lambda^{1/2}(s, m_1^2, s_2)}\,\mathrm{d}t_1, \quad \text{or}$$
$$\mathrm{d}\Phi_2(s_2, m_2^2, m_3^2) = \frac{\lambda^{1/2}(s_2, m_2^2, m_3^2)}{8s_2}\,\mathrm{d}\Omega_3. \tag{5}$$

Both forms for $\mathrm{d}\Phi_2$ are equivalent because of the relation between the four-momentum transfer and the scattering angle for the 2-body scattering process. Here $\Omega_3$ is the solid scattering angle of particle 3 in the $\{23\}$ rest frame. In principle, in the $\{23\}$ rest frame the orientation of the momentum vector $\mathbf{p}_3$ can be expressed by the vector $\mathbf{p}_b$ as well as by $\mathbf{p}_1$. The first selection corresponds to the Jackson frame while selecting $\mathbf{p}_1$ corresponds to the helicity frame.

Equation (5) indicates the physical meaning of the solid angle $\Omega_3$ for the diagrams depicted in fig. 1 and naturally defines the axis $\mathbf{p}_b$ along which the angular distribution of particle 3 should be measured in the rest frame $\{23\}$. This solid angle is defined as $\Omega_{3b}$. Indeed, considering the subprocess $x + b \to 2 + 3$ it is clear that any resonance structure appearing in the $\{23\}$ subsystem will be directly reflected in the angular distribution in the Jackson frame. With respect to $\Omega_{3b}$ the differential cross-section is given by

$$\frac{\mathrm{d}\sigma}{\mathrm{d}s_2\mathrm{d}t_1\mathrm{d}\Omega_{3b}} = \frac{\lambda^{1/2}(s_2, m_2^2, m_3^2)}{2^{10}\pi^4\lambda(s, m_a^2, m_b^2)s_2}|\mathcal{M}(s, s_2, t_1, \Omega_{3b})|^2. \tag{6}$$

The polar angle of $\Omega_{3b}$ is called Jackson angle $\theta_{3b}$ [43,44], while the azimuthal angle $\phi_{3b}$ was originally defined by Treiman and Yang [45]. The relation between the Jackson angle and the invariants is given by

$$\cos\theta_{3b} = \frac{2s_2(t_2-m_b^2-m_3^2)+(s_2+m_b^2-t_1)(s_2+m_3^2-m_2^2)}{\lambda^{1/2}(s_2,m_b^2,t_1)\,\lambda^{1/2}(s_2,m_3^2,m_2^2)}, \tag{7}$$

which follows from the definition of $t_2$ in eq. (1) when considering the reaction $x+b \to 2+3$. If the $x+b \to 2+3$ amplitude does not depend on $\Omega_{3b}$, the angular distribution $\mathrm{d}\sigma/\mathrm{d}\Omega_{3b}$ in the Jackson frame is isotropic. The angular distribution reflects the $\Omega_{3b}$-dependence of the elementary $x+b \to 2+3$ reaction amplitude. It is important that due to the symmetry of the reaction with respect to the beam and target nucleon the Jackson angle is likewise given along the beam axis, *i.e.* particle $b$ can be replaced by $a$ in the previous formulation. Moreover, considering the production of the $\{23\}$ subsystem in a specific spin state one can parameterize the decay angular distribution $\mathrm{d}\sigma/\mathrm{d}\Omega_{3b}$ in terms of the spin density matrix [44–46].

The helicity frame defines the solid angle $\Omega_{31}$ with $\theta_{31}$ being called the helicity polar angle, while $\lambda_{31}$ is the corresponding azimuthal angle. The helicity frame can be naturally explained by considering the Dalitz plot representation. The solid angle $\Omega_{31}$ appears through an extension of the invariant mass $s_3 = (P_1+P_3)^2$ in the frame specified by $P_2+P_3 = (P_a+P_b)-P_3 = (\sqrt{s_2},\mathbf{0})$, *i.e.* in the $\{23\}$ rest frame. The helicity polar angle is then given by

$$\cos\theta_{31} = \frac{2s_2(m_1^2+m_2^2-s_1)+(s-s_2-m_1^2)(s_2+m_2-m_3)}{\lambda^{1/2}(s,s_2,m_1^2)\lambda^{1/2}(s_2,m_2^2,m_3^2)} \tag{8}$$

and is contained in the Dalitz plot. For fixed $s_2$ the allowed range of $s_1$ is given by eq. (8) with $\cos\theta_{31} = \pm 1$. Actually, eq. (8) defines the contour of the Dalitz plot in the $s_1$ *versus* $s_2$ plane. Any anisotropy in the helicity polar-angle distribution is not necessarily a signature for the appearance of higher partial waves in the final system. Rather, it reflects structures in the invariant mass spectra of the $\{12\}$ and $\{23\}$ subsystems. Indeed, for any fixed value of $s_2$ it is possible to project the Dalitz plot into the $s_1$ distribution, which can be converted into a $\theta_{31}$ distribution by eq. (8). The same can be done also for the $s_2$ projection.

Generally speaking, the helicity angle depends only on the kinematics of the final state while the Jackson angle is a function of both the initial- and final-state kinematics.

The Chew-Low plot is obtained by integration of eq. (6) with respect to the solid angle $\Omega_{3b}$ and yields

$$\frac{\mathrm{d}\sigma}{\mathrm{d}s_2\mathrm{d}t_1} = \frac{\lambda^{1/2}(s_2,m_2^2,m_3^2)}{2^8\pi^3\lambda(s,m_a^2,m_b^2)s_2}\,|\mathcal{M}(s,s_2,t_1)|^2\,, \tag{9}$$

assuming that the matrix element does not depend on $\Omega_{3b}$ (or $\Omega_{31}$). The Chew-Low presentation is the most convenient way for the evaluation of the reaction cross-section. It allows to account for the $t_1$-dependence of the reaction amplitude via the operator structure of the vertex, the propagator and the form factors, as well as of the mass structure in only one of the final two-body subsystems.

## 3 The reaction amplitude

We consider the target $a$ as a spin-(1/2) particle and the exchange of a spin-less boson $x$ with mass $\mu$. At this stage we do not account for the FSI. The most general form of the production amplitude is then given by

$$\mathcal{M} = \frac{f_{a1x}}{\mu}\,F(t_1)\,\bar{u}(p_1)\mathcal{O}u(p_a)\,\frac{\mathcal{A}_{xb\to 23}(s_2,t_2)}{t_1-\mu^2}\,, \tag{10}$$

where $f_{a1x}$ is the coupling constant of the $a1x$ vertex and $F(t_1)$ is the form factor at this vertex. The operator $\mathcal{O}$ is $\gamma_5$ or 1 depending on the parity of the exchanged boson. For $\pi$, $\eta$, $\eta'$, etc. exchanges it is $\gamma_5$, while for $\sigma$, $a_0$, $f_0$ exchanges it is just 1. The quantity $\mathcal{A}_{xb\to 23}$ is the invariant amplitude for the process $x+b \to 2+3$. It is related to the physical scattering amplitude and can be parametrized through

$$|\mathcal{A}_{\pi N\to K\Lambda}|^2 = 64\pi^2 s_{K\Lambda}\,\left[\frac{\lambda(s_{K\Lambda},m_\pi^2,m_N^2)}{\lambda(s_{K\Lambda},m_K^2,m_\Lambda^2)}\right]^{1/2}\frac{\mathrm{d}\sigma}{\mathrm{d}\Omega},$$
$$|\mathcal{A}_{KN\to KN}|^2 = 64\pi^2 s_{KN}\,\frac{\mathrm{d}\sigma}{\mathrm{d}\Omega}, \tag{11}$$

by utilizing existing differential cross-section data for the two amplitudes in question. In this equation $s_{K\Lambda}$ and $s_{KN}$ are the squared invariant energies of the $K\Lambda$ or $KN$ subsystems, respectively, while $m_N$, $m_K$ and $m_\Lambda$ are the masses of the nucleon, the kaon and the $\Lambda$-hyperon. Since the data determine only the on-shell values of $\mathcal{A}_{KN\to KN}$ and $\mathcal{A}_{\pi N\to K\Lambda}$ the off-shellness of the amplitude in eq. (10) has to be taken into account. The minimal modification of the on-shell amplitude to account for this is to include a form factor.

In any case, the $x+b \to 2+3$ invariant scattering amplitude can be expressed in terms of partial waves via [47]

$$\mathcal{A}_{xb\to 23} = 8\pi\sqrt{s_2}\,\chi_f^+\left[f_1+\frac{(\boldsymbol{\sigma}\cdot\mathbf{q}_f)(\boldsymbol{\sigma}\cdot\mathbf{q}_i)}{q_f q_i}\,f_2\right]\chi_i, \tag{12}$$

where $f_1$ and $f_2$ are defined by

$$f_1 = \sum_{l=1}^{\infty}[T_{l-1}^+(s_2) - T_{l+1}^-(s_2)]P_l'(\cos\theta)\,,$$
$$f_2 = \sum_{l=1}^{\infty}[T_l^-(s_2) - T_l^+(s_2)]P_l'(\cos\theta)\,. \tag{13}$$

Here $l$ is the orbital angular momentum of the final state, $P_l'(\cos\theta)$ is the derivative of the Legendre polynomial $P_l(\cos\theta)$, and $\theta$ is the scattering angle in the $x+b \to 2+3$ center-of-mass (cm) system. Note that $T_l^+$ and $T_l^-$ are the partial-wave (PW) amplitudes corresponding to the total angular momentum $J = l \pm 1/2$. In eq. (12) $\chi_i$ and $\chi_f$ are the two-dimensional Pauli spinors of initial and final fermions and $\boldsymbol{\sigma}$ are the Pauli spin matrices. Furthermore, $\mathbf{q}_i$ and $\mathbf{q}_f$ are the cm momenta of the initial and final states whose moduli are given by

$$q_i^2 = \frac{\lambda(s_2,m_x^2,m_b^2)}{4s_2}, \qquad q_f^2 = \frac{\lambda(s_2,m_2^2,m_3^2)}{4s_2} \tag{14}$$

for on-shell scattering. The $x+b \to 2+3$ differential cross-section in terms of the invariant amplitude is

$$\frac{\mathrm{d}\sigma}{\mathrm{d}\Omega} = \frac{1}{64\pi^2 s}\,\frac{q_f}{q_i}\,|\mathcal{A}_{xb\to 23}|^2, \tag{15}$$

while in terms of the amplitudes $F = f_1 + f_2\cos\theta$ and $G = -f_2\sin\theta$ it is given by

$$\frac{\mathrm{d}\sigma}{\mathrm{d}\Omega} = \frac{q_f}{q_i}\,(|F|^2+|G|^2)\,. \tag{16}$$

$F$ and $G$ are the non-flip and spin-flip amplitudes, respectively, and their partial-wave representations read

$$\begin{aligned} F &= \sum_{l=0}^{\infty}[(l+1)T_l^+ + lT_l^-]\,P_l(\cos\theta), \\ G &= \sum_{l=1}^{\infty}\sin\theta\,[T_l^+ - T_l^-]\,P_l'(\cos\theta). \end{aligned} \tag{17}$$

For the computation of the $\pi$- and $K$-meson exchange mechanisms we need the elementary $K^+p \to K^+p$ and $\pi^0 p \to K^+\Lambda$ amplitudes and also the parameters of the corresponding pion and kaon emission vertices ($\pi NN$ and $\Lambda NK$ coupling constants and cut-off mass of the pertinent vertex form factors), cf. diagrams a) and b) in fig. 1. The elementary $KN \to KN$ and $\pi N \to K\Lambda$ amplitudes are specified in the next sections. With regard to the couplings $f$ we use the standard relation to the (pseudoscalar) coupling constants $g$,

$$f_{\pi NN} = g_{\pi NN}\frac{m_\pi}{2m_N}, \quad f_{\Lambda NK} = g_{\Lambda NK}\frac{m_K}{2\sqrt{m_N m_\Lambda}}\,, \tag{18}$$

and we take the value $g_{\pi NN}$=13.45. The $\Lambda NK$ coupling constant is fixed by applying standard $SU(3)$ symmetry relations,

$$g_{\Lambda NK} = -g_{\pi NN}\frac{1+2\alpha}{\sqrt{3}}, \tag{19}$$

where $\alpha$ is the $F$ to $D$ ratio, $\alpha = F/(F+D)$. Adopting the quark model estimate of $\alpha = 2/5$ together with $g_{\pi NN}$ specified above we obtain $g_{\Lambda NK} = -13.98$. We furnish the $\pi NN$ and $\Lambda NK$ vertices with monopole form factors

$$F(t_1) = \frac{\Lambda_x^2 - \mu^2}{\Lambda_x^2 - t_1}, \tag{20}$$

utilizing different cut-off masses for the $\pi$- and $K$-meson exchanges. These cut-off masses are considered as free parameters and are adjusted to the data. For COSY energies, the exact form of this form factor is not important.

In phenomological approaches the relative phase between the amplitudes is not fixed so that the total reaction amplitude is given by

$$\mathcal{M} = \mathcal{M}_K + \mathcal{M}_\pi e^{i\psi}\,, \tag{21}$$

where $\psi$ can, in principle, depend on the energy. The importance of the relative phase or, more generally speaking, the role of interference effects between the $\pi$- and $K$-meson exchange remains so far unclear. In the $\pi + K$ calculations of refs. [6,48] it was found that $K$-meson exchange dominates the reaction $pp \to pK^+\Lambda$ and the interference was neglected. Later on the role of interference effects was exploited in ref. [49] in a study of the $pp \to pK^+\Lambda$ to $pp \to pK^+\Sigma^0$ cross-section ratio. But also in this work it was concluded that the reaction $pp \to pK^+\Lambda$ itself is insensitive to the interference, because it is dominated by $K$-meson exchange. Here we study the $\pi$- and $K$-meson exchanges separately, *i.e.* we do not add the amplitudes as indicated by eq. (21) and therefore the uncertainty of the relative phase $\psi$ is not relevant for the present investigation.

## 4 The KN → KN amplitude

We use the $KN$ amplitude of the Jülich meson-exchange model. A detailed description of the model is given in refs. [50,51]. The model yields a satisfactory description of the available experimental data on elastic and charge exchange $KN$ scattering including angular spectra and polarization observables up to a $KN$ invariant mass of $\sqrt{s_2} \simeq 2$ GeV. For the analysis of the $pp \to pK^+\Lambda$ reaction only the $K^+p \to K^+p$ scattering amplitude is necessary. Figure 2 shows the differential cross-section for elastic $K^+p$ scattering at different invariant energies. The strong forward peaking of the data and in the calculation comes

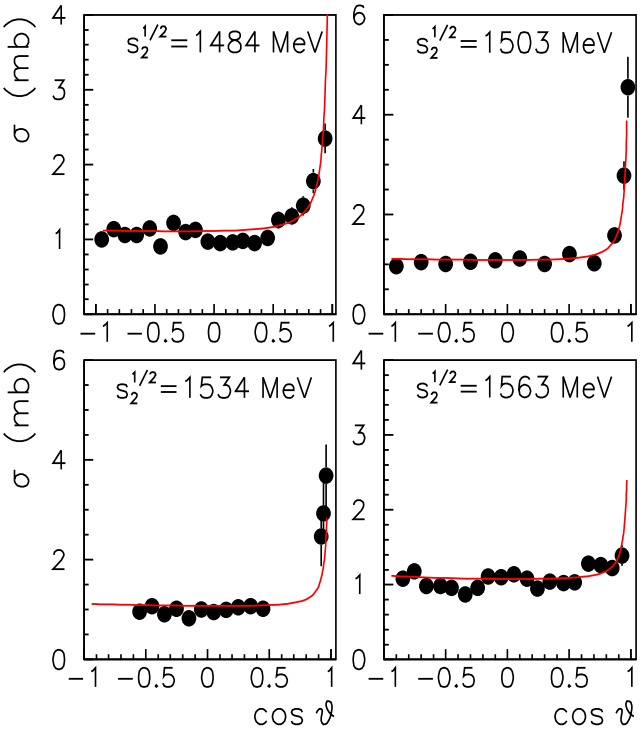


**Fig. 2.** Differential cross-sections of the reaction $K^+p \to K^+p$ in the center-of-mass system at different invariant collision energies. The solid lines show the results from the Jülich model [51]. The data are from ref. [68].

from the Coulomb interaction. Apart of this peaking the angular spectra are isotropic indicating a dominance of the $s$-wave amplitude in the $K^+p \to K^+p$ reaction.

Note that the $KN$ amplitude of the Jülich model was extensively used recently for imposing limits of the $\Theta^+$ pentaquark width from data on the reaction $K^+d \to K^0pp$ [52,53] and for an analysis of the DIANA results [54] where the $\Theta^+$ was observated in $K^+$-meson collisions with Xe nuclei [55].

For the evaluation of the $K$ exchange contribution to the reaction $pp \to pK^+\Lambda$ one needs the $KN$ amplitude for the energy range $m_K + m_N \le \sqrt{s_2} \le \sqrt{2m_N(2m_N + T)} - m_\Lambda$, where $T$ is the proton beam energy. The energy at COSY is limited to $T \le 2.88\,\mathrm{GeV}$ which means that $\sqrt{s_2} \le 1.9\,\mathrm{GeV}$. Thus, the energy range for which the $KN$ model of the Jülich group was designed is sufficient to analyze data in the COSY regime. However, in order to connect with data for $pp \to pK^+\Lambda$ at higher energies, specifically with total cross-sections, one needs to know the $KN$ scattering amplitude at $\sqrt{s_2} > 1.8\,\mathrm{GeV}$. Here we adopt a phenomenological approach and parameterize the $KN$ scattering amplitude by experimental data [56–59] utilizing eq. (11).

## 5 The πN ⟶ KΛ amplitude

The Jülich $\pi N$ model [60] currently does not include the coupling to the $K\Lambda$ channel, therefore we use the PW analysis of Sotona and Zofka [61]. Their amplitudes contain ($s$-channel) resonances as well as $t$-channel $K^*$-meson exchange and other background contributions. The PW amplitudes are given in ref. [61] up to $\sqrt{s_2} = 2.3\,\mathrm{GeV}$. For the analysis of data in the COSY regime we need the $\pi N \to K\Lambda$ amplitude up to $\sqrt{s_2} \le 2.05\,\mathrm{GeV}$. At higher energies the available $\pi N \to K\Lambda$ data (differential cross-sections and $\Lambda$-hyperon recoil polarization) can be reproduced by $K^*$-meson exchange alone taking into account absorptive corrections [62–65]. Thus, we extend the amplitude of Sotona and Zofka appropriately so that we can study the $pp \to pK^+\Lambda$ reaction cross-section over a larger energy range and consider data collected at COSY as well as those available at higher energies. The non-flip and spin-flip amplitudes for the $K^*$-meson exchange is taken from ref. [66] with parameters listed in ref. [61]. In order to reproduce the available data for $\sqrt{s_2} > 2.3\,\mathrm{GeV}$ we readjust the coupling constants for the $K^*$-meson exchange to $g_0 = -24.0$ and $g_1 = -83.3$ as compared to those from ref. [61].

Figure 3 shows the total $\pi^-p \to K^0\Lambda$ reaction cross-section as a function of the invariant collision energy [67]. The solid line is the result with the PW amplitudes of ref. [61]. Obviously, the data below 2.3 GeV are fairly well described. The dashed line indicates the contribution from the $K^*$-meson exchange, which dominates the reaction above invariant energies of about 2 GeV.

A typical feature of the $\pi N \to K\Lambda$ reaction is the strong angular asymmetry and the large $\Lambda$-hyperon polarization which occurs already at energies close to the reaction threshold. Corresponding experimental results are

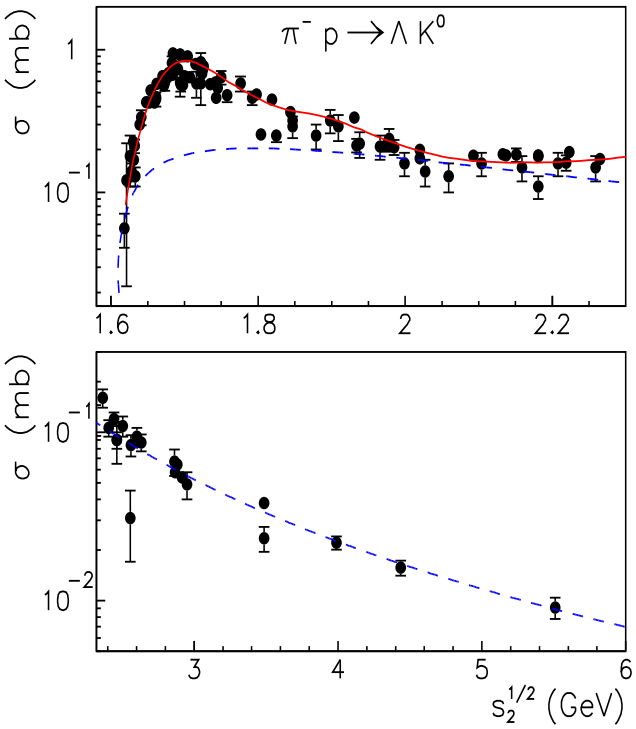


**Fig. 3.** Total $\pi^-p \to K^0\Lambda$ reaction cross-section as a function of the invariant collision energy. The data are taken from ref. [67]. The solid line is the result based on the PW amplitudes of ref. [61] while the dashed line shows the contribution from the $K^*$-meson exchange.

shown in figs. 4 and 5 where the squares are data from Knasel *et al.* [68], while the circles are from the experiment of Baker *et al.* [69]. Evidently, the polarization is already nonzero at $\sqrt{s_2} = 1633\,\mathrm{MeV}$, the lowest-energy where data are available, which corresponds to an excess energy of only $\epsilon = 19.67\,\mathrm{MeV}$. The recoil polarization is defined as

$$P = \frac{2\Im(FG^*)}{|F|^2 + |G|^2}\,, \tag{22}$$

where the spin-nonflip ($F$) and spin-flip ($G$) amplitudes are given in eq. (17) in terms of the PW amplitudes. The $s$-wave alone results in zero recoil polarization, while the $p$-wave alone results in a strong angular dependence of the polarization. Note that above $\sqrt{s_2} \simeq 1.8\,\mathrm{GeV}$ the $\Lambda$-hyperon recoil polarization starts to show a stronger angle dependence and a change of sign appears at a certain $\cos\theta$. Let us mention also that $P$ does not vanish even at energies as high as $\sqrt{s_2} = 3.2\,\mathrm{GeV}$ (which is the maximal energy where polarization data are available).

The solid lines in figs. 4 and 5 are the results based on the full PW amplitude of ref. [61], while the dashed lines indicate results obtained with inclusion of the resonances only. It is clear that the nonresonant background plays a significant role already at energies close to the reaction threshold and is essential for a quantitative reproduction of the differential observables.

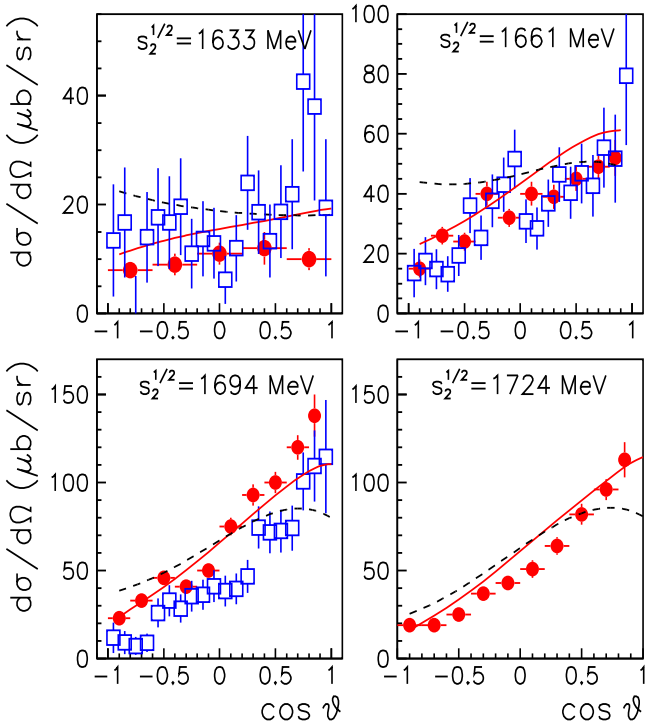


**Fig. 4.** Differential cross-sections for the reaction $\pi^- p \to K^0\Lambda$ in the center-of-mass system at different invariant collision energies. The solid lines are results based on the full PW amplitudes of ref. [61]. The dashed lines are obtained when only the resonant contributions are taken into account. The squares are data from ref. [68], while the circles are from ref. [69].

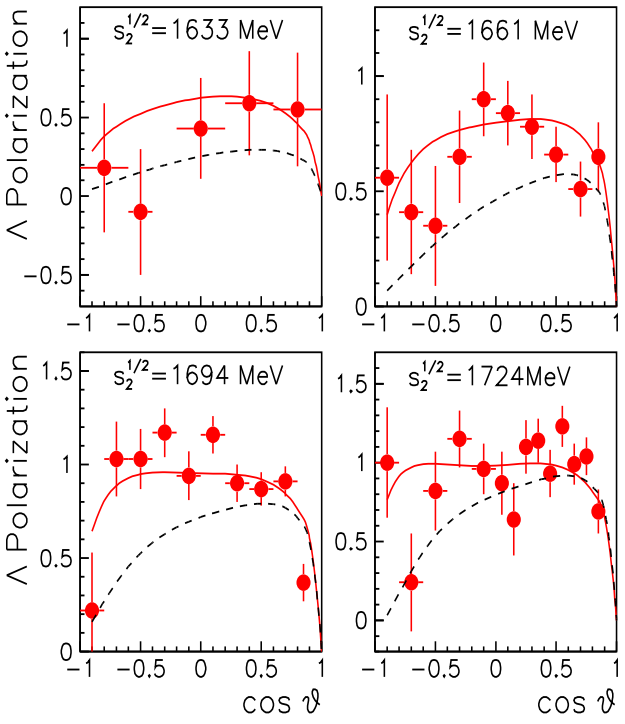


**Fig. 5.** $\Lambda$ polarizations for the reaction $\pi^- p \to K^0\Lambda$ in the center-of-mass system at different invariant collision energies. Same description as in fig. 4.

One can see from fig. 4 that there is partly an inconsistency between the two data sets and it is obvious that the PW analysis cannot reproduce simultaneously both sets of data. We should say that there are also polarization data by Knasel *et al.* [68] for the energy $\sqrt{s_2} = 1633\,\mathrm{MeV}$. However, the error bars of these data are so large that they are not useful for our analysis. As a consequence, they are not shown in fig. 5.

The structure of the elementary $\pi N \to K\Lambda$ amplitude suggests that a measurement of the invariant $K\Lambda$ mass spectra and the angular correlations according to eqs. (7), and (8) might allow to isolate the contribution of the $\pi$ exchange to the $pp \to pK^+\Lambda$ reaction. However, it is possible that due to the short-ranged nature of the strangeness production reaction higher partial waves in the virtual $\pi N \to K\Lambda$ amplitude are suppresed so that the $s$-wave dominates the $pp \to pK^+\Lambda$ observables at COSY energies. In that case the angular correlation of eq. (7) from $\pi$- and $K$-meson exchanges would be similar and the relevant spectrum should be isotropic. But it should be still possible to detect any $s$-wave resonance in the $K\Lambda$ system through an analysis of the Dalitz plot distribution and the angular correlation of eq. (8). We will come back to this issue below.

## 6 The Λp final-state interaction

Production reactions like $NN \to K^+\Lambda N$ require a large momentum transfer between the initial and final baryons. Thus, the range of the production mechanism will be much smaller than the characteristic range of the interactions in the final states. In such a case the energy dependence of the reaction amplitude is driven primarily by that of the scattering amplitude of the outgoing particles and it was proposed [70] to factorize the reaction amplitude

$$\mathcal{M} \to \mathcal{M} \times \mathcal{A}_{FSI}, \tag{23}$$

where $\mathcal{A}_{FSI}$ denotes the amplitude due to the interaction between the final particles. $\mathcal{A}_{FSI}$ is in principle a 3-body amplitude. However, it is generally assumed that the $\Lambda p$ interaction dominates over the other possible final-state interactions and therefore one replaces $\mathcal{A}_{FSI}$ by $\mathcal{A}_{\Lambda p}$. The validity of this assumption is to some extent questionable. It is based primarily on the observation that the absolute value of the $\Lambda p$ scattering length is substantially larger than those for $K^+p$ and $K^+\Lambda$ scattering, although one has to admit that the latter is actually not known. In any case, very close to the reaction threshold the relative momenta between all final particles are small and one should account for the interference between the FSI in the various two-body systems. In that kinematics the interference term between the large and small scattering lengths might be not negligible. For instance in the analysis [71,72] of the $\gamma d \to pn\eta$ reaction very close to the reaction threshold, *i.e.* at $\epsilon < 20\,\mathrm{MeV}$ it was found that the $NN$ and $\eta N$ final-state interactions interfere. But in the present investigation we concentrate on excess energies in the order

of 100 MeV and, therefore, the simplification in the FSI treatment should be justified.

According to the above arguments the near-threshold mass dependence of the $\Lambda p$ spectrum for the $pp \to pK^+\Lambda$ reaction might be dominated by the energy dependence of the $\Lambda p$ scattering amplitude. Since the range of the $\Lambda p$ invariant mass is from $m_\Lambda + m_N$ to $\epsilon + m_\Lambda + m_N$ FSI effects should be visible in differential observables at any collision energy. On the other hand, in case of the total reaction cross-section FSI effects should be dominantly seen at energies close to the reaction threshold. At higher energies the FSI affects only a small part of the available phase space [73,74], *i.e.* only the region where the relative momenta of the $\Lambda p$ system are sufficiently small and, therefore, have a comparably low weight in the integration over the whole phase space.

A very simple treatment of FSI effects was proposed by Watson [75] and Migdal [76]. Close to the reaction threshold the invariant scattering amplitude is dominated by the $s$-wave and can be expressed in terms of the effective range expansion as

$$\mathcal{A}_{\Lambda p}(q) = N_0(m_\Lambda + m_N)\left[-\frac{1}{a} + \frac{rq^2}{2} - iq\right]^{-1}, \qquad (24)$$

where $a$ and $r$ are the scattering length and the effective range, respectively, and $q$ is the relative momentum between the $\Lambda$ hyperon and final proton,

$$q = \frac{\lambda^{1/2}(s_{\Lambda p}, m_\Lambda^2, m_p^2)}{2\sqrt{s_{\Lambda p}}}. \qquad (25)$$

$N_0$ is a normalization constant, which cannot be fixed within the Watson-Migdal approximation.

While the Watson-Migdal prescription is well applicable to final-state interactions that are characterized by a large scattering length like in case of the $NN$ interaction, say, this is not true for $\Lambda p$ where the expected scattering lengths are only in the order of one to two fermi [36]. Here one should resort at least to the so-called Jost function approach which was found in ref. [36] to yield resonable qualitative results. For a $\Lambda p$ scattering amplitude that is given by the effective-range approximation, cf. eq. (24), over the whole energy range, the FSI factor in the Jost function approach can be evaluated analytically and amounts to

$$\mathcal{A}_{\Lambda p}(q) = \frac{q + i\beta}{q - i\alpha}, \qquad (26)$$

where $\alpha$ and $\beta$ are related to the scattering parameters via

$$a = \frac{\alpha + \beta}{\alpha\beta}, \qquad r = \frac{2}{\alpha + \beta} \qquad (27)$$

with $\alpha < 0$ and $\beta > 0$. In our notation the scattering length $a$ is defined with a negative sign, cf. eq. (24), which explains the difference to the formulas given by Goldberger and Watson [70]. Equation (26) implies the limits

$$\lim_{q\to 0} \mathcal{A}_{\Lambda p}(q) = -\frac{\beta}{\alpha}, \qquad \lim_{q\to\infty} \mathcal{A}_{\Lambda p}(q) = 1, \qquad (28)$$

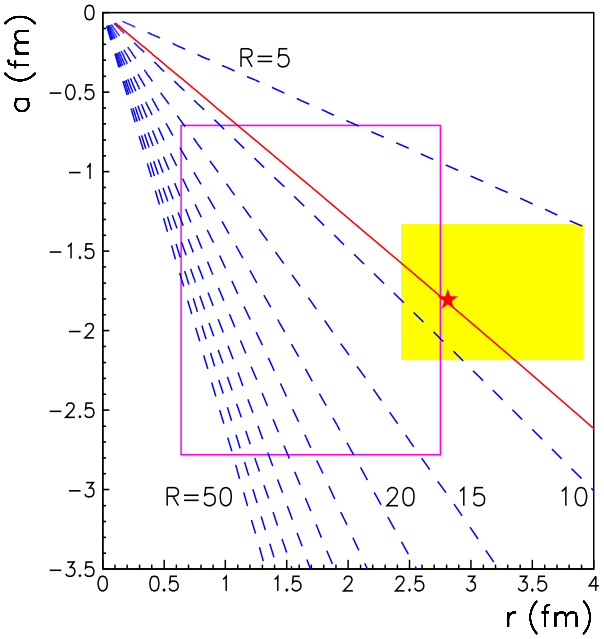


**Fig. 6.** The enhancement factor $R$ (cf. eq. (30)) as a function of the $\Lambda p$ effective range $r$ and scattering length $a$. The dashed lines show results for $R = 5$–$50$ calculated at $\epsilon = 2$ MeV. The hatched (open) box indicates the range of $r$ and $a$ for the $\Lambda p$ interaction in the triplet (singlet) state, taken from refs. [38–40]. The star indicates the parameters used in our analysis, while the solid line shows the family of $r$ and $a$ resulting in $R = 8.7$.

which can be used as a measure for the relative strength of the FSI with respect to the contribution from the processes without FSI. Equation (26) can be written in the form

$$\mathcal{A}_{\Lambda p}(q) = \left[\frac{r\beta^2}{2} + \frac{rq^2}{2}\right]\left[-\frac{1}{a} + \frac{rq^2}{2} - iq\right]^{-1}, \qquad (29)$$

which at small $q$ is close to the Watson-Migdal parameterization of eq. (24) (apart from the unknown normalization constant $N_0$). In addition, the Jost function approach also includes the correct behavior for large momenta, cf. eq. (28).

At present a solid estimation of FSI effects for the reaction $pp \to pK^+\Lambda$ is difficult because of two reasons: a) the $\Lambda p$ system can be in the singlet and triplet states that can have different effective-range parameters $a$ and $r$. It is not known whether the $\Lambda p$ system is predominantly produced in one or the other state. We should mention though that most microscopic models of the reaction $pp \to pK^+\Lambda$ predict a dominance of the triplet contribution. b) The effective range parameters are not well known, *i.e.* they are afflicted with large uncertainties. This is visualized in fig. 6 where the hatched box shows the range of $r$ and $a$, for the triplet case, taken from some recent $YN$ potential models [38–40]. The open box in fig. 6 indicates the variation in the singlet effective-range parameters. It is clear that the uncertainties of the $\Lambda p$ interaction allow a large freedom of FSI effects in the reaction $pp \to pK^+\Lambda$.

In order to illustrate how strongly the FSI with different scattering parameters might influence the $pp \to pK^+\Lambda$ reaction cross-section, we evaluate the so-called enhancement factor $R$ as a function of the excess energy. $R$ is defined as the integral of $|\mathcal{A}_{\Lambda p}(q)|^2$ from eq. (26) over the nonrelativistic 3-body phase space, normalized to the phase space volume $\Phi_3$, *i.e.*

$$R(\epsilon) = \frac{1}{\Phi_3} \int_0^{\sqrt{2\mu\epsilon}} \sqrt{2\tilde{\mu}\left(\epsilon - \frac{q^2}{2\mu}\right)}\, \frac{q^2+\beta^2}{q^2+\alpha^2}\, q^2\, \mathrm{d}q$$
$$= 1 + \frac{4\beta^2 - 4\alpha^2}{(-\alpha + \sqrt{\alpha^2 + 2\mu\epsilon})^2}, \qquad (30)$$

where $\mu$ and $\tilde{\mu}$ are reduced masses given by

$$\mu = \frac{m_\Lambda m_N}{m_\Lambda + m_N}, \qquad \tilde{\mu} = \frac{m_K(m_\Lambda + m_N)}{m_K + m_\Lambda + m_N}, \qquad (31)$$

and $\Phi_3$ is given by the integral of eq. (30) without the factor $|\mathcal{A}(q)|^2$ from eq. (26).

The dashed lines in fig. 6 show the enhancement factor $R$ for the specific excess energy $\epsilon = 2\,\mathrm{MeV}$, as a function of the effective range and scattering length. One can see that the variations of the $\Lambda p$ triplet parameters in refs. [38–40] exclude any values $R > 12$. On the other hand, the singlet parameters allow for almost any magnitude of the enhancement factor. As just mentioned above, most microscopic models of the reaction $pp \to pK^+\Lambda$ favour the triplet contribution. In our analysis we do not consider singlet and triplet $\Lambda p$ FSI effects separately but use averaged parameters fixed to the value shown in fig. 6 by the star [37].

## 7 The pp → pK⁺Λ reaction cross-section

Figure 7 shows the $pp \to pK^+\Lambda$ reaction cross-section as a function of the excess energy. The squares represent data that were available before the COSY aera collected in ref. [67]. The circles are from measurements at the COSY facility, performed by the COSY-11 [16,17,21] and TOF Collaborations [23]. Apparently the COSY experiments provide a substantial contribution to the data base, specifically they are the only source of information for the behaviour of the cross-section near the reaction threshold.

For a general overview it is always useful to compare the data to the phase space behaviour, *i.e.* to consider the given reaction kinematics but set the reaction amplitude to $\mathcal{M} = \text{const}$. In case of the total reaction cross-section the relevant kinematics is the dependence of the 3-body phase space on the excess energy, which in the nonrelativistic case[1] is given by eq. (30). The integration can be performed analytically and yields

$$\sigma(\epsilon) = \frac{\sqrt{m_K m_N m_\Lambda}}{2^7\pi^2(m_K+m_N+m_\Lambda)^{3/2}} \frac{\epsilon^2}{\sqrt{s^2 - 4sm_N^2}} |\mathcal{M}|^2\,. \quad (32)$$

[1] Actually, the nonrelativistic and the relativistic phase space for the reaction $pp \to pK^+\Lambda$ are almost identical for $\epsilon < 2\,\mathrm{GeV}$.

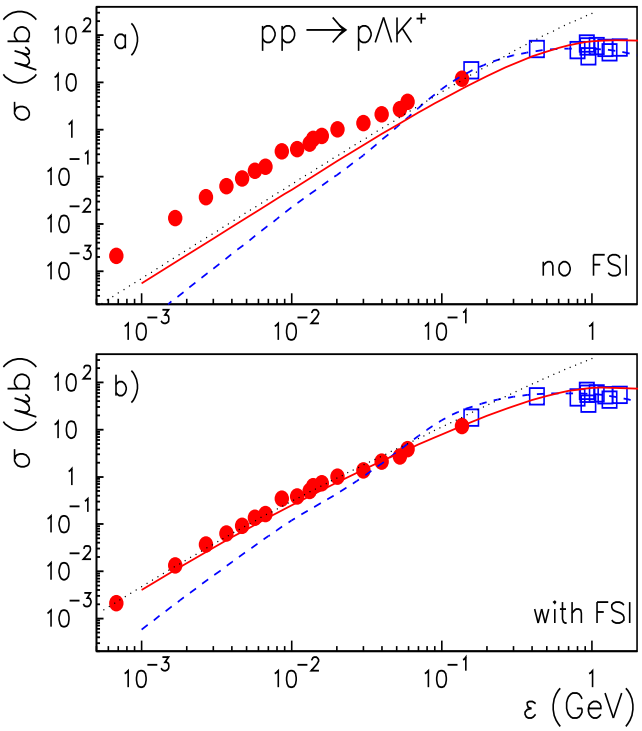


**Fig. 7.** Total cross-section for the reaction $pp \to pK^+\Lambda$ as a function of the excess energy. The upper figure shows results without FSI, while for the lower figure the $\Lambda p$ FSI was included via eq. (26). The solid lines are results for the $K$-meson exchange mechanism. The dashed lines are obtained with $\pi$-meson exchange and with the full $\pi N \to K\Lambda$ transition amplitude. The dotted lines show results for a constant reaction amplitude $\mathcal{M}$ without (a) and with (b) FSI effects. The squares are data taken from ref. [67], while the circles are from experiments at the COSY facility [16,17,21,23].

This results is shown by the dotted line in fig. 7a) for the squared invariant amplitude $|\mathcal{M}|^2 = 2.2 \cdot 10^7\ \mu\mathrm{b}$, which was normalized to the data at $\epsilon \simeq 130\,\mathrm{MeV}$. Following the discussion given in sect. 6 one expects that close to the threshold the data deviate from a calculation that neglects the $\Lambda p$ FSI, and this is indeed the case, cf. fig. 7a). For example, at $\epsilon \simeq 2\,\mathrm{MeV}$ the phase space line underestimates the data by a factor of around 9.

When we now introduce FSI effects within the Jost function approach, eq. (26), we can easily reproduce the energy dependence of the data by adopting the parameters

$$\beta = 212.7\,\mathrm{MeV} \quad \text{and} \quad \alpha = -72.3\,\mathrm{MeV}, \qquad (33)$$

which correspond to the low-energy parameters $a = -1.8\,\mathrm{fm}$ and $r = 2.8\,\mathrm{fm}$. The resulting cross-section is shown by the dotted line in fig. 7b).

The employed low-energy parameters are indicated in fig. 6 by a star. Obviously, they are well within the present uncertainty range of the triplet parameters. But we would like to emphasize that any (singlet or triplet) combination of effective-range parameters that lies on the solid line of fig. 6 would give similar results, *i.e.* would re-

produce the energy dependence observed in the experiment. There is no unique solution. Thus, the presented specific fit does not provide any deeper understanding of the strangeness production mechanism or the hyperon-nucleon interaction. It only illustrates that any reaction mechanism, which implies a sufficiently weak energy dependence, would be compatible with the empirical information.

Let us now come to concrete reaction mechanisms. The solid line in fig. 7a) shows the result for $K$-meson exchange without FSI. In our calculation the $s_{KN}$- and $t_2$-dependence of the $KN \to KN$ scattering amplitude, the $t_1$-dependence of the propagator and the $KN\Lambda$ vertex and formfactor and the $s_{\Lambda p}$-dependence of the FSI (cf. below) is taken into account and we perform a full four-dimensional integration of eq. (2). The results were normalized to the data at $\epsilon \simeq 1\,\mathrm{GeV}$ by adjusting the cut-off mass of the form factor eq. (20) to $\Lambda \simeq 1.7\,\mathrm{GeV}$. In contrast to the pure phase space, the $K$-meson exchange well reproduces the energy dependence of the data also at high energies, which will be discussed later. The results obtained with the FSI of eq. (26) utilizing the parameters of eq. (33) are shown by the solid line in fig. 7b). It is interesting to see that the results for $K$-meson exchange are practically identical to the phase space behaviour over a large energy range.

Results for the $\pi$ exchange mechanism are shown by the dashed line in fig. 7a), for the case without $\Lambda p$ FSI. Again, we normalize our results at $\epsilon \simeq 1\,\mathrm{GeV}$ by adjusting the cut-off mass to $\Lambda \simeq 1.6\,\mathrm{GeV}$. It is evident that the energy dependence predicted by the $\pi$-meson exchange differs from the one resulting from $K$-meson exchange and the phase space calculations. As a consequence, the calculation with FSI (dashed line in fig. 7b)), substantially underestimates the data below $\epsilon = 200\,\mathrm{MeV}$.

In order to shed light on the difference in the energy dependence of the total cross-sections resulting from $K$- and $\pi$-meson exchange let us take a look at the elementary $\pi N \to K\Lambda$ amplitude $\mathcal{A}_{\pi N\to K\Lambda}$. The square of this amplitude can be obtained from data via eq. (11). It is shown in fig. 8. Here the angular dependence is integrated out so that the amplitude depends only on the invariant collision energy $s_{K\Lambda}$ or the final momentum $q_f$, respectively. The experimental results (solid circles) are cross-section data taken from ref. [67], divided appropriately by phase space factors. It is evident that $|\mathcal{A}_{\pi N\to K\Lambda}|^2$ is strongly energy dependent. Specifically, it does not exhibit the behaviour of a standard $s$-wave amplitude, which would be constant in the near-threshold region, nor that of a $p$-wave, which should be proportional to $q_f^2$. Rather the data seem to rise linearly with the moment $q_f$, cf. the dotted line in fig. 8.

According to the PW analysis of ref. [61] the reaction $\pi N \to K\Lambda$ is dominated by the $S_{11}(1650)$ and $P_{11}(1710)$ resonances for energies up to $\sqrt{s_{K\Lambda}} \simeq 1.8\,\mathrm{GeV}$, as discussed in sect. 5. These resonance amplitudes, $\mathcal{A}^R_{\pi N\to K\Lambda}$, are given by [61]

$$\mathcal{A}^R_{\pi N\to K\Lambda} = -\frac{8\pi\sqrt{s_{K\Lambda}}}{q_i q_f}\,\frac{\sqrt{\Gamma_{\pi N}\Gamma_{K\Lambda}}\,M_R\Gamma}{M_R^2 - s_{K\Lambda} - i f M_R\Gamma}, \qquad (34)$$

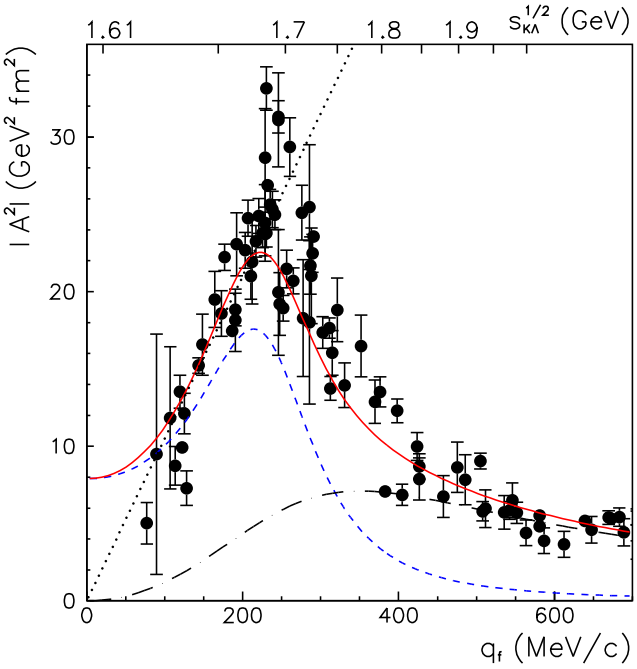


**Fig. 8.** The $\pi N \to K\Lambda$ amplitude squared as a function of the final momentum $q_f$ and the invariant collision energy $s_{K\Lambda}$ (axis at the top). The dashed and dash-dotted lines show the contribution from the $S_{11}$ and $P_{11}$ resonances, respectively, of the PW analysis presented in ref. [61]. Their sum corresponds to the solid line. The dotted line indicates the $q_f$-dependence. The circles are experimental results, extracted from the data given in ref. [67], cf. text.

where $M_R$ and $\Gamma$ are the mass and full width of the resonance,

$$f = \frac{\delta}{100} f_f^l + \frac{100-\delta}{100} f_i^l,$$
$$f_i^l = \frac{\phi_l(R\,q_i)\;q_i}{\phi_l(R\,q_i^R)\;q_i^R}, \qquad f_f^l = \frac{\phi_l(R\,q_f)\;q_f}{\phi_l(R\,q_f^R)\;q_f^R}, \qquad (35)$$

and the initial and final momenta are

$$q_i^2 = \frac{\lambda(s_{K\Lambda}, m_{\pi^2}, m_N^2)}{4 s_{K\Lambda}}, \qquad q_f^2 = \frac{\lambda(s_{K\Lambda}, m_K^2, m_\Lambda^2)}{4 s_{K\Lambda}}. \qquad (36)$$

$q_i^R$ and $q_f^R$ are the corresponding momenta at the resonance pole position, *i.e.* at $\sqrt{s_{K\Lambda}} = M_R$. The interaction radius was taken as $R = 1.696\,\mathrm{GeV}^{-1}$. The function $\phi_l$ ensures the correct threshold energy dependence and is given by [69,77,78]

$$\phi_0(x) = 1, \qquad \phi_1(x) = \frac{x^2}{1+x^2}, \qquad (37)$$

for $s$ and $p$ waves, respectively. Finally, the partial decay width was parametrized by

$$\sqrt{\Gamma_{\pi N}\Gamma_{K\Lambda}} = B\sqrt{f_f^l f_i^l}. \qquad (38)$$

In the following calculations we use the $S_{11}$- and $P_{11}$-resonance parameters as fixed by the PW analysis of

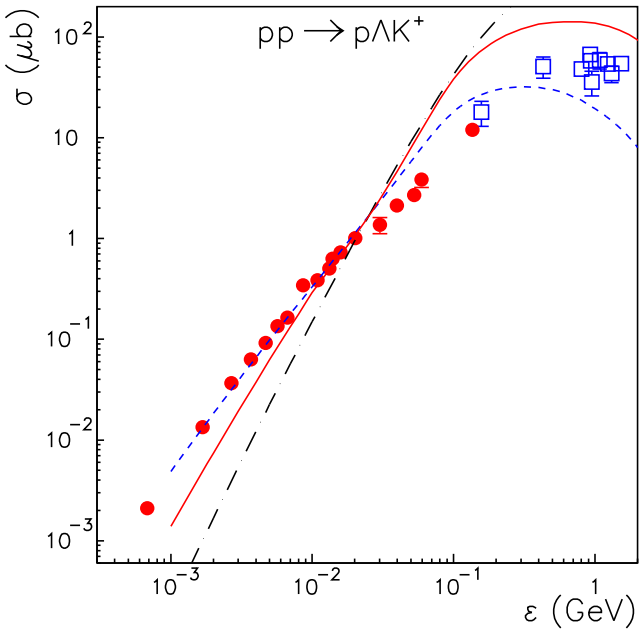


**Fig. 9.** Total cross-section for the reaction $pp \to pK^+\Lambda$ as a function of the excess energy. The dashed line is the result for the $\pi$-meson exchange mechanism with the $S_{11}(1650)$-resonance amplitude, while the dashed-dotted line was obtained with the $P_{11}(1710)$-resonance alone. The solid line shows the full calculation. In all cases the $\Lambda p$ FSI is taken into account via eq. (26) with parameters specified in eq. (33). For comparison the lines are normalized at the same excess energy. The squares are data taken from ref. [67], while the circles are from experiments at the COSY facility [16,17,21,23].

ref. [61] which we already introduced in the sect. 5. Specifically, we use for the $S_{11}(1650)$-resonance

$$M_R = 1678\,\text{MeV}, \qquad \Gamma = 117\,\text{MeV}, \\ B = 0.2175, \qquad \delta = 7.8855, \tag{39}$$

and for the $P_{11}(1710)$-resonance

$$M_R = 1730\,\text{MeV}, \qquad \Gamma = 543\,\text{MeV}, \\ B = 0.1565, \qquad \delta = 12.893. \tag{40}$$

The square of these resonance amplitudes are shown in fig. 8 by the dashed ($S_{11}$) and dash-dotted lines ($P_{11}$), respectively. The solid line is the sum of these two contributions which illustrates that those two resonances together indeed reproduce the bulk of the experimental amplitude.

Predictions for the $pp \to pK^+\Lambda$ cross-section utilizing the pion exchange mechanism with the $S_{11}$ or $P_{11}$ resonances are shown in fig. 9 by the solid and dashed lines, respectively. The $\Lambda p$ FSI is included via eq. (26) with the parameters specified in eq. (33). It is obvious that the energy dependence of the calculation based on the $P_{11}$-resonance differs substantially from the experiment. The curve obtained for the $S_{11}$-resonance is in good agreement with the data for $\epsilon < 40\,\text{MeV}$, but deviates at higher energies.

The results discussed above make clear that, in contrast to the $K$-meson exchange scenario, the pion exchange mechanism yields a much stronger energy dependence of the production cross-section, due to the excitation of resonances. However, it would be premature to see the individual disagreement of the $S_{11}$ as well as of the $P_{11}$ case with the energy dependence of the data as an evidence for a $K$-meson exchange dominance of the $pp \to pK^+\Lambda$ reaction. Indeed, by exploiting the freedom in the interplay between the $S_{11}(1650)$ and $P_{11}(1710)$ resonances it is still possible to reproduce the cross-section data over a large energy range, as is well illustrated in refs. [24–26]. To discern between the two scenarios considered here ($K$ *versus* $\pi$ exchange) one must consider differential observables like those introduced in sect. 2. Corresponding results will be discussed in the next two sections.

Before that we want to comment on the $t_1$-dependence. For that purpose we consider the Chew-Low integration of eq. (9) with the reaction amplitude $\mathcal{M}_\pi$ neglecting the FSI, *i.e.* the $s_{\Lambda p}$-dependence. After integrating over $t_2$ or $\cos\theta_{3b}$ (see fig. 1 and eq. (7)) the $pp \to pK^+\Lambda$ reaction cross-section due to $\pi$-meson exchange is given by

$$\sigma(\epsilon) = \frac{g^2_{\pi NN}}{2^8\pi^2(s^2-2sm_N^2)} \int_{s_-}^{s_+} \mathrm{d}s_{K\Lambda} \int_{t_-}^{t_+} \mathrm{d}t_1 \frac{\lambda^{1/2}(s_{K\Lambda}, m_K^2, m_\Lambda^2)}{s_{K\Lambda}} \\ \times \frac{-t_1}{(t_1-m_\pi^2)^2} \left[\frac{\Lambda^2-m_\pi^2}{\Lambda^2-t_1}\right]^2 |\mathcal{A}_{\pi N\to K\Lambda}(s_{K\Lambda})|^2, \tag{41}$$

where $t_1$ is the squared four-momentum transferred from the initial to the final proton and the limits of integrations are

$$s_- = (m_K+m_\Lambda)^2, \qquad s_+ = (m_K+m_\Lambda+\epsilon)^2, \\ t_\pm = 2m_N^2 - \frac{s+s_{K\Lambda}-m_N^2}{2} \\ \pm \frac{\sqrt{s-4m_N^2}\ \lambda^{1/2}(s, s_{K\Lambda}, m_N^2)}{2\sqrt{s}}. \tag{42}$$

For cut-off masses in the order of $\Lambda = 1.6\,\text{GeV}$ the $t_1$-dependence of eq. (41) becomes significant only for $t_1 > -0.3\,\text{GeV}^2$, which is accessible only at $\epsilon \geq 200\,\text{MeV}$. Indeed, at threshold

$$t_\pm = m_N(m_N - m_K - m_\Lambda) \simeq -0.63\,\text{GeV}^2, \tag{43}$$

so that for energies not too far from the threshold the reaction cross-section depends only very weakly on $t_1$. Therefore, for pion exchange —but in fact, also for kaon exchange— the $t_1$-dependence of the reaction amplitude $\mathcal{M}$ is almost negligible for excess energies $\epsilon < 200\,\text{MeV}$. Only for energies around $\epsilon \approx 1\,\text{GeV}$ and above the $t_1$-dependence becomes noticable. Then the squared reaction amplitude is significantly reduced so that, after integration over the 3-body phase space, a perfect description of the reaction cross-section at higher energies is achieved for $\pi$ as well as for $K$ exchange, in contrast to the calculation where $\mathcal{M} = \text{const}$, cf. the corresponding results in fig. 7.

This observation suggest that a completely differential treatment of the reaction $pp \to pK^+\Lambda$ within the four-dimensional space of eq. (2) is not necessary, because in

any case the very smooth $t_1$-dependence does not provide access to conclusive information about the vertex function, the propagator of the exchange particles and the form factor for bombarding energies within the COSY regime.

## 8 The Dalitz plot

The Dalitz plot for the reaction $pp \to pK^+\Lambda$ at the excess energy $\epsilon = 130$ MeV is presented in fig. 10. The results are based on the $K$-meson exchange mechanism with inclusion of the $\Lambda p$ FSI. We consider the excess energy $\epsilon = 130$ MeV because we found that this is more or less the optimal minimal energy where a separation between the FSI effects and the $S_{11}$-resonance is still possible. Of course, for the $K$-meson exchange mechanism only the structure coming from the $\Lambda p$ FSI is detectable in the Dalitz plot distribution at low $s_{\Lambda p}$ and there is no visible structure due to the $K\Lambda$ subsystem. Recall that for a constant reaction amplitude $\mathcal{M} = $ const the distribution is isotropic. In case of a $K$-meson exchange dominance the experimental Dalitz plot should resemble the result shown in fig. 10.

The projections of the Dalitz, *i.e.* the squared invariant mass spectra in the $K\Lambda$ and $\Lambda p$ subsystems, are shown in fig. 11. The solid histograms are calculations for the $K$-meson exchange mechanism including the $\Lambda p$ FSI given by eq. (26). The dashed lines indicate the phase space distribution, which results from the integration of the Dalitz plot of eq. (3) over one of the invariant mass squared. For the $\Lambda p$ subsystem the squared invariant mass spectrum is

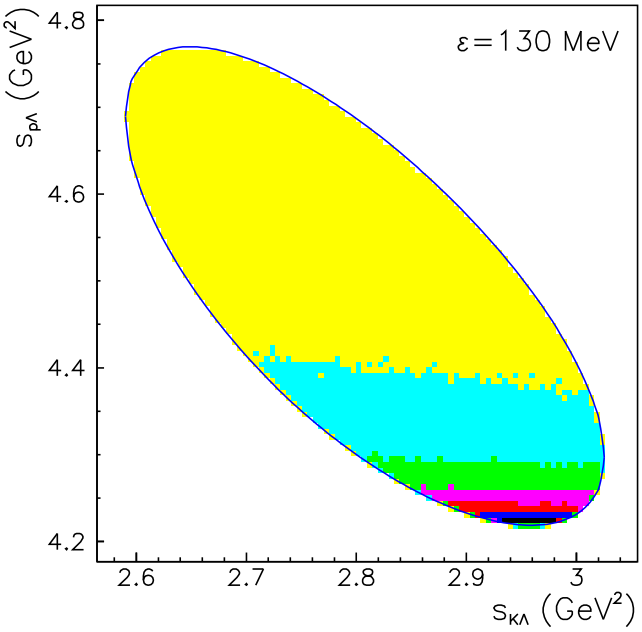


**Fig. 10.** The Dalitz plot distribution for the reaction $pp \to pK^+\Lambda$ at the excess energy $\epsilon = 130$ MeV as a function of the invariant mass squared $s_{K\Lambda}$ and $s_{\Lambda p}$. The shown result is for the $K$-meson exchange mechanism including the $\Lambda p$ FSI. The solid contour is the Dalitz plot boundary given by the helicity angle $\cos\theta_{31} = \pm 1$ of eq. (8).

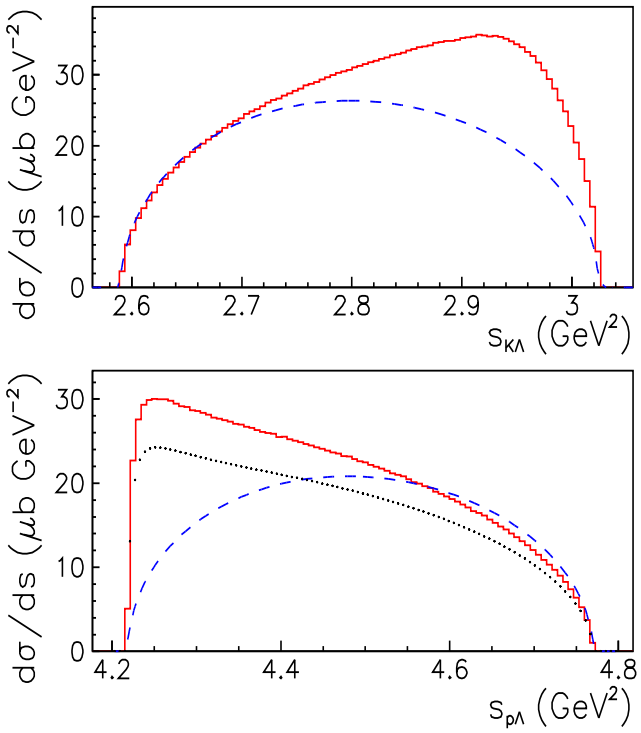


**Fig. 11.** The $s_{K\Lambda}$ and $s_{\Lambda p}$ invariant mass spectra for the reaction $pp \to pK^+\Lambda$ at $\epsilon$=130 MeV. The solid histograms show the $K$-meson exchange calculations with inclusion of the $\Lambda p$ FSI. The dashed lines indicate the phase space distribution given by eq. (44), while the dotted line is the phase space distribution multiplied by the FSI amplitude $|\mathcal{A}_{\Lambda p}|^2$ from eq. (26). The dashed and dotted lines are shown in arbitrary normalization.

given by

$$\frac{\mathrm{d}\sigma}{\mathrm{d}s_{\Lambda p}} = \frac{\lambda^{1/2}(s, s_{\Lambda p}, m_K^2)\,\lambda^{1/2}(s_{\Lambda p}, m_\Lambda^2, m_p^2)}{2^8\pi^3\, s\,\sqrt{s^2 - 4sm_N^2}\, s_{\Lambda p}}\,|\mathcal{M}|^2, \quad (44)$$

where $|\mathcal{M}|^2 = $ const. The $K\Lambda$ distribution can be easily obtained in a similar way. The phase space distributions in fig. 11 are arbitrarily normalized. As compared to the phase space the result for the $K$-meson exchange mechanism indicates an enhancement at low $\Lambda p$ masses. At the same time the $K\Lambda$ distribution is enhanced at large masses, which results from the kinematic reflection. We should emphasize, however, that the enhancement comes practically only from the $\Lambda p$ FSI.

Let us now compare the full $K$-meson exchange calculation with the simple FSI factorization approach given by the product of the phase space distribution from eq. (44) and the $\Lambda p$ FSI amplitude $|\mathcal{A}_{\Lambda p}|^2$ of eq. (26). Corresponding results are shown by the dotted line in fig. 11. The latter was slightly renormalized in order to make it optically distinguishable from the (solid) histogram. One can see that the $\Lambda p$ spectrum obtained by factorization of the FSI and phase space practically coincides with the full calculation. This demonstrates that in case of an almost constant reaction amplitude the $\Lambda p$ distribution can be savely used for the evaluation of the hyperon-nucleon scattering pa-

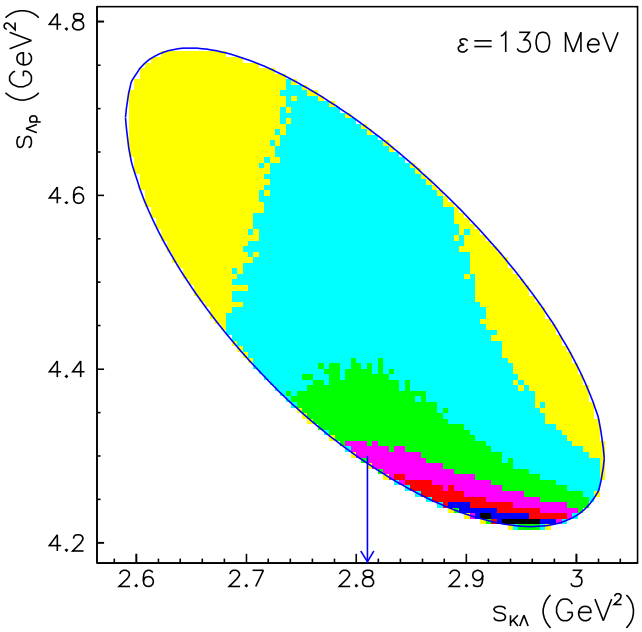


**Fig. 12.** The Dalitz plot distribution for the reaction $pp \to pK^+\Lambda$ at $\epsilon = 130$ MeV as a function of the invariant mass squared $s_{K\Lambda}$ and $s_{\Lambda p}$. The shown result is for the $\pi$ exchange mechanism with excitation of the $S_{11}(1650)$-resonance and includes also the $\Lambda p$ FSI. The solid contour is the Dalitz plot boundary given by eq. (8). The arrow indicates the square of the $S_{11}(1650)$-resonance mass.

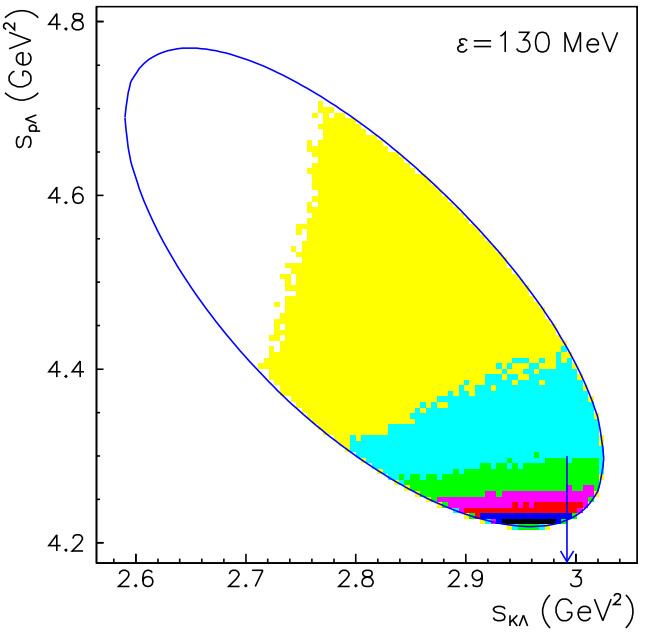


**Fig. 13.** The Dalitz plot distribution for the reaction $pp \to pK^+\Lambda$ at $\epsilon = 130$ MeV as a function of the invariant mass squared $s_{K\Lambda}$ and $s_{\Lambda p}$. The shown result is for the $\pi$ exchange mechanism with excitation of the $P_{11}(1710)$-resonance and includes also the $\Lambda p$ FSI. The solid contour is the Dalitz plot boundary given by eq. (8). The arrow indicates the squared of the $P_{11}(1710)$-resonance mass.

rameters, as was done in refs. [33,34]. Note, however, that there is still a theoretical uncertainty involved in such an evaluation depending strongly on the method applied [36]. In any case it is clear that, if $K$-meson exchange dominates the $pp \to pK^+\Lambda$ reaction, then this could be unambigously deduced from the Dalitz plot.

Now we turn to the $\pi$-meson exchange mechanism and the excitation of baryonic resonances in the $\pi N \to K\Lambda$ reaction. The resonances can be recognized by a Breit-Wigner-type shape in the $\Lambda K$ invariant mass spectrum and by the angular dependence of the $S_{11}(1650)$ and $P_{11}(1710)$ decay products, which is determined by the resonance spin and production mechanism [41]. But one needs to distinguish the resonances in the $\Lambda K$ subsystem from the $\Lambda p$ FSI, because the latter mimics a resonance-like structure in the $\Lambda p$ subsystem with a pole at $m_\Lambda + m_N$ and width given roughly by the $\Lambda p$ scattering parameters. Therefore, it is necessary to consider the complete Dalitz plot distribution. However, if the baryonic resonances and the FSI overlap we should return to the completely differential treatment in the four-dimensional space given by eq. (2), *i.e.* consider the $t_1$ as well as the $t_2$ invariants.

The Dalitz plot distribution for the $\pi$-meson exchange mechanism, with excitation of the $S_{11}(1650)$-resonance and inclusion of the $\Lambda p$ FSI, is shown in fig. 12. The distribution substantially differs from the result obtained for the $K$-meson exchange scenario. Specifically, the influence of the resonance can be clearly seen. The arrow in fig. 12 indicates the resonance position, *i.e.* the square of the resonance mass. A sufficiently large excess energy like $\epsilon = 130$ MeV allows to separate the effects due to the $S_{11}(1650)$-resonance and the $\Lambda p$ FSI, which is important for the data evaluation. The situation is different for $\pi$-meson exchange and $P_{11}(1710)$ excitation, shown in fig. 13. Here the signal of the $P_{11}$-resonance overlaps with the $\Lambda p$ FSI. In principle, even in this case the Dalitz plot might be sufficient to reconstruct the resonance contribution but it would be more promising to perform a combined Dalitz plot and $t_2$ or Jackson angle analysis. Of course, such an analysis requires large experimental statistics.

Since there are now structures in the $K\Lambda$ as well as $\Lambda p$ subsystems one might expect a substantial distortion of the Dalitz-plot projections. This issue is addressed in fig. 14 where we show the $s_{K\Lambda}$ and $s_{\Lambda p}$ invariant mass spectra. The solid histograms are the full results for the $\pi$-meson exchange mechanism, with excitation of the $S_{11}(1650)$-resonance and including the $\Lambda p$ FSI, while the dashed lines indicate the phase space distributions given by eq. (44). The dash-dotted line in fig. 14b) corresponds to the phase space distribution multiplied by the FSI amplitude, $|\mathcal{A}_{\Lambda p}|^2$, from eq. (26). Obviously, and opposite to the $K$-meson exchange scenario discussed above, now the factorization in terms of the $\Lambda p$ FSI and the phase space deviates significantly from the full calculation. The presence of the $S_{11}(1650)$-resonance changes the $\Lambda p$ invariant mass spectra. This observation should be kept in mind when analyzing the invariant mass spectra given by the

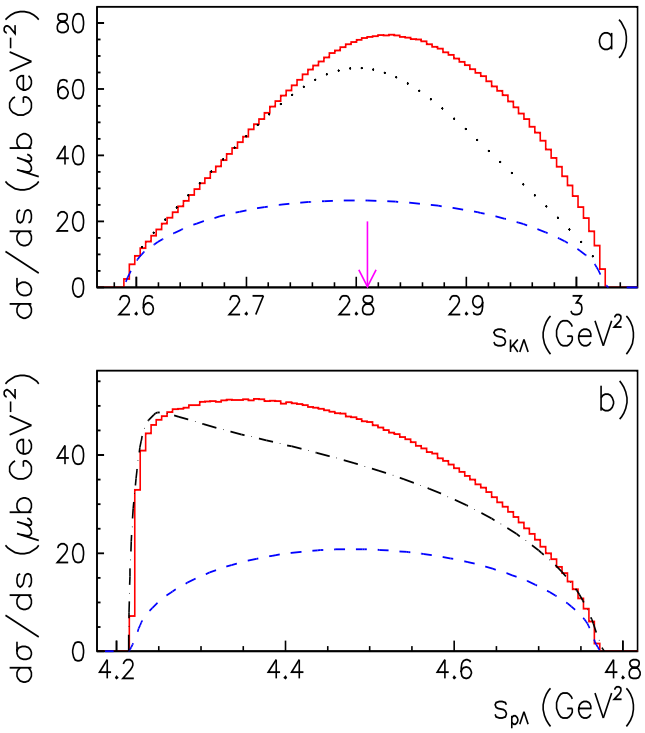


**Fig. 14.** The $s_{K\Lambda}$ and $s_{\Lambda p}$ squared invariant mass spectra for the reaction $pp \to pK^+\Lambda$ at $\epsilon = 130$ MeV. The solid histograms show the $\pi$-meson exchange calculation with inclusion of the $S_{11}(1650)$-resonance and the $\Lambda p$ FSI. The dashed lines indicate the phase space distribution given by eq. (44). The dotted line in a) is the phase space distribution multiplied by the squared $S_{11}$ resonant amplitude given by eq. (34). The dash-dotted line in b) is the phase space distribution multiplied by the squared FSI amplitude $|\mathcal{A}_{\Lambda p}|^2$ from eq. (26). The dashed and dotted lines are shown with arbitrary normalization. The arrow indicate the squared mass of the $S_{11}(1650)$-resonance.

projection of the Dalitz plot distribution with the aim to extract the $\Lambda p$ effective-range parameters from the FSI. *A priori* the full structure of the reaction amplitude and the effects due to possible kinematic reflections in the different final subsystems are not known. Thus, one should rather consider slices of the Dalitz plot than projections for the aforementioned analysis in order to be on the safe side —though this again requires larger experimental statistics.

The dotted line in fig. 14a) is the phase space distribution multiplied by the square of the $S_{11}(1650)$ amplitude, cf. eq. (34). Again this result differs significantly from the full $\pi$-meson exchange calculation because of the kinematic reflection of the $\Lambda p$ FSI. Indeed, the enhancement with respect to the results obtained by factorization at large $s_{K\Lambda}$ stems entirely from the FSI.

## 9 Angular correlations

As was discussed in sect. 2 the angular correlations are given by eq. (7) in the Jackson frame and by eq. (8) in the helicity frame. While the former angular spectra, *i.e.* the Jackson and Treiman-Yang angular distributions, contain information directly related to the partial-wave decomposition of the reaction amplitude, this is not the case for the helicity angle distributions. Specifically, an anisotropy in the latter distributions is not necessarily a signature for contributions of higher partial waves, as already pointed out in sect. 2.

With regard to the dependence of the reaction amplitude on the $t_1$ invariant we concluded already in sect. 7 that it should be rather smooth for $\epsilon < 200$ MeV for $\pi$ as well as for $K$ exchange. Therefore, in this energy range the $t_1$-dependence is not a good tool to distinguish between different production mechanisms.

In case of the $K$-meson exchange mechanism the $t_2$-dependence is related to the $KN$ scattering amplitude. Since $K^+p$ elastic scattering is dominated by the $s$-wave one would expect an isotropic distribution of the Jackson angle of eq. (7). However, the situation should be very different for the $pn \to pK^0\Lambda$ reaction which involves the $K^+n \to K^0p$ subprocess. Due to the strong angular dependence of the charge exchange amplitude, which originates from the isospin $I = 0$ component, the Jackson angle distribution should exhibit $p$-wave contributions [53].

For the $\pi$-meson exchange mechanism the $t_2$ distribution contains the angular dependence of the $\pi N \to K\Lambda$ transition amplitude and can be converted by eq. (7) to the angular spectrum in the Jackson frame. If the $S_{11}(1650)$-resonance dominates the reaction the Jackson angle distribution is isotropic, *i.e.* similar to that resulting from the $K^+$-meson exchange scenario. If the $\pi N \to K\Lambda$ amplitude is given entirely by the $P_{11}(1710)$-resonance, the Jackson angle distribution is again isotropic, which is obvious from eqs. (16) and (17). Finally, if both $S_{11}$ and $P_{11}$ resonances contribute to the $pp \to pK^+\Lambda$ reaction then the Jackson angle distribution would show the interference between the $s$ and $p$ waves given by eqs. (12) and (13). A proper analysis of the angular distribution would then allow to extract the relative contributions of these resonances.

The angular distribution in the helicity frame just give the projection of the Dalitz plot as a function of the squared invariant mass of a particular subsystem while the squared invariant mass of the other subsystem is fixed. For the reaction $pp \to pK^+\Lambda$ one can study the $\Lambda p$ invariant mass spectra at a fixed or partially integrated squared invariant mass of the $K\Lambda$ subsystem. Since $s_{K\Lambda}$ is fixed one can transform, by eq. (8), the $s_{\Lambda p}$ distribution to the helicity angle distribution. That allows to present the data in a more convenient way because $-1 \leq \cos\theta_{31} \leq 1$. But one should remember that the helicity angle distribution is just a slice of the Dalitz plot and it does not contain more information than the Dalitz plot itself. We discuss the usefulness of the helicity angle spectra now.

Figure 15 shows the $\Lambda p$ helicity angle distribution for different intervals of the squared invariant mass of the $K\Lambda$ subsystem, for the reaction $pp \to pK^+\Lambda$ at $\epsilon = 130$ MeV. Note that according to eq. (8) the maximal $\Lambda p$ mass corresponds to forward helicity angles. The solid histograms are

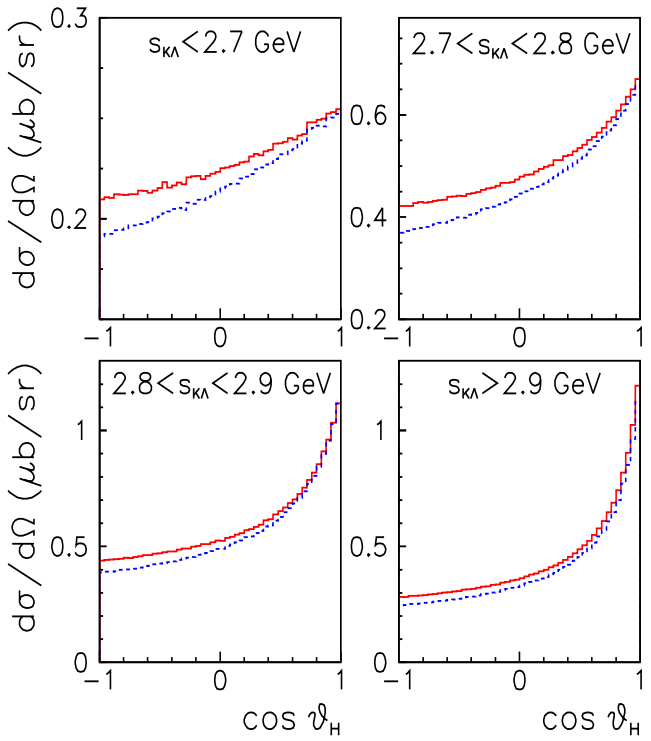


**Fig. 15.** The $\Lambda p$ helicity angle spectra at different squared invariant masses of the $K\Lambda$ subsystem, $s_{K\Lambda}$, for the reaction $pp \to pK^+\Lambda$ at $\epsilon = 130\,\mathrm{MeV}$. The solid histograms show the $\pi$-meson exchange calculation with inclusion of the $S_{11}(1650)$-resonance and the $\Lambda p$ FSI. The dashed histograms are the corresponding results for the $K$-meson exchange mechanism.

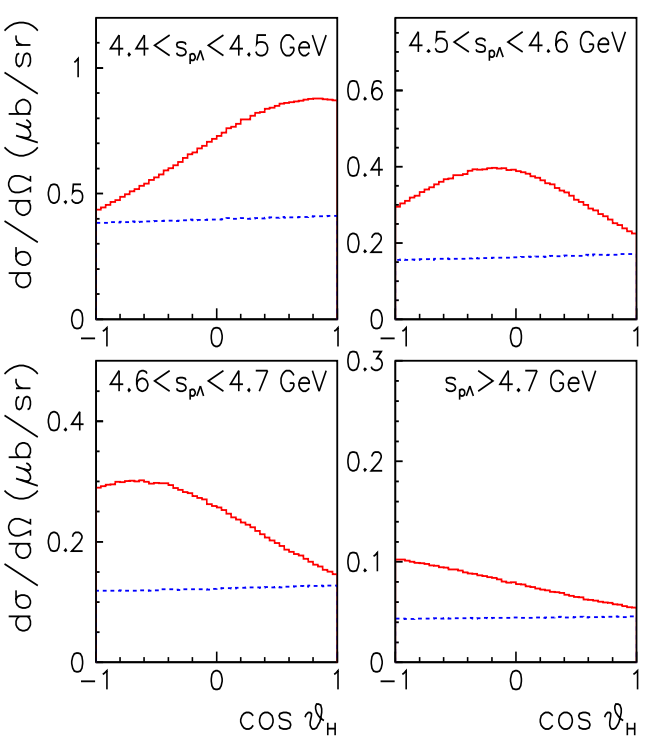


**Fig. 16.** The $K\Lambda$ helicity angle spectra at different squared invariant masses of the $\Lambda p$ subsystem, $s_{\Lambda p}$, for the reaction $pp \to pK^+\Lambda$ at $\epsilon = 130\,\mathrm{MeV}$. The solid histograms show the $\pi$-meson exchange calculations with inclusion of the $S_{11}(1650)$-resonance and the $\Lambda p$ FSI. The dashed histograms are the corresponding results for the $K$-meson exchange mechanism.

results obtained for the $\pi$-meson exchange scenario with $S_{11}(1650)$ excitation and with $\Lambda p$ FSI, while the dashed histograms are results for the $K$-meson exchange mechanism. It is obvious that these distributions are excellent observables for the extraction of the $\Lambda p$ effective-range parameters, since by performing cuts on $s_{K\Lambda}$ one can strongly reduce the influence of that part of the Dalitz plot which is distorted by the resonance. Of course, for a separation of the singlet and triplet parameters corresponding spin-dependent experiments need to be performed and one should apply reliable extraction methods like the one advocated in ref. [36], based on dispersion theory.

Figure 16 shows the $K\Lambda$ helicity angle distribution for different intervals of the squared invariant mass of the $\Lambda p$ subsystem. Again the calculations were done at $\epsilon = 130\,\mathrm{MeV}$ and for the $\pi$-meson exchange mechanism with the $S_{11}$-resonance and the $\Lambda p$ FSI (solid histograms) and also for the $K$-meson exchange mechanims (dashed histograms). We explicitly cut the $\Lambda p$ FSI region by taking the distributions only for $s_{\Lambda p} > 4.4\,\mathrm{GeV}^2$. Now the spectra show the $S_{11}(1650)$-resonance structure whereas they do not show any structure in case of the $K$-meson exchange. Thus, if there is any structure these spectra might be fitted by a resonance amplitude, *i.e.* a Breit-Wigner form say, in order to determine the resonance mass and width. Moreover, the fitting procedure can be applied at different intervals of $s_{\Lambda p}$ following eq. (8). The procedure should provide resonance parameters independently of the range $s_{\Lambda p}$ if the FSI region is properly cut. Indeed, fitting as a test the calculated $K\Lambda$ helicity angle spectrum at $4.6 < s_{\Lambda p} < 4.7\,\mathrm{GeV}^2$ we obtained the resonance parameters $M_R = 1.672\,\mathrm{GeV}$ and $\Gamma = 116.6\,\mathrm{MeV}$. These resonance parameters are close to those given by eq. (39), *i.e.* those used for the actual calculation with the $\pi$-meson exchange mechanism. We examined the procedure by allowing an admixture of contributions from the $K$-meson exchange mechanism. It turned out that the extraction of the resonance parameters from the helicity angle distributions yields quite stable results.

## 10 Summary

We presented a study of the strangeness production reaction $pp \to pK^+\Lambda$ for the energy range accessible at high-luminosity accelerator facilities like COSY. All relevant observables of the reaction for unpolarized beam and target nucleons are discussed in terms of their dependence on the final four independent invariants. The reaction amplitude is constructed by considering the $\pi$- as well as $K$-meson exchange production mechanisms and employing elementary $KN \to KN$ and $\pi N \to K\Lambda$ transition amplitudes taken from a microscopic model ($KN$)

and a partial-wave analysis ($\pi N \to K\Lambda$). Effects of the $\Lambda p$ final-state interaction are included too by means of the so-called Jost function approach.

Though our analysis utilizes only $\pi$- and $K$-meson exchange we would like to emphasize that the results are, in fact, more general. All predictions given for the considered spin-independent observables for the $\pi$-meson exchange mechanism, say, would be practically the same for any other nonstrange meson exchange, *i.e.* for the $\sigma$, $\eta$, $\rho$ mesons. The quantum numbers and the masses of the exchange particle are reflected in the dependence on the squared four-momentum $t_1$ transferred from the initial to the final nucleon. However, the range of $t_1$ accessible in experiments with excess energies up to $\epsilon \approx 150\,\mathrm{MeV}$, say, is simply too small for generating any noticeable differences in the studied observables. Thus, the two production mechanisms examined in the present investigation can be considered as representatives of two general classes of reaction scenarios, namely where either a nonstrange or strange meson is exchanged in the production process. At the same time this means, of course, that unpolarized experiments within this energy region will not allow to discriminate more specifically between different production mechanisms.

We addressed the questions whether the considered observables can be used to determine the $\Lambda p$ interaction or to identify resonances that couple to the $K\Lambda$ channel. It was found that the Dalitz plot and its sliced projections or the helicity angle spectra are indeed useful for extracting specific information on the $\Lambda p$ interaction and possible baryonic resonances in the $K\Lambda$ subsystem. The Jackson angle distribution is a crucial tool to study the onset of higher partial waves in the $KN \to KN$ and $\pi N \to K\Lambda$ transition amplitudes. Specifically, if the reaction is dominated by the $S_{11}(1650)$-resonance we expect zero $\Lambda$-hyperon recoil polarization and an isotropic distribution of the Jackson angle. When both $S_{11}$ and $P_{11}$ resonances contribute the Jackson angle distribution should show an interference as well as recoil polarization. Furthermore, the Dalitz plot would explicitly indicate the resonance structure in the $K\Lambda$ system and at sufficiently large excess energy like $\epsilon = 130\,\mathrm{MeV}$ the $S_{11}(1650)$-resonance effects can be well isolated from the $\Lambda p$ FSI.

We proposed to study specifically the $K\Lambda$ helicity angle spectra at large $\Lambda p$ masses squared, $s_{\Lambda p} > 4.4\,\mathrm{GeV}^2$, (in order to eliminate effects of the $\Lambda p$ FSI) for a reliable determination of ($S_{11}(1650)$) resonance parameters. We also pointed out that the $\Lambda p$ effective-range parameters could be most reliably extracted from the $\Lambda p$ helicity angle spectra with cuts $s_{K\Lambda} > 2.9\,\mathrm{GeV}^2$.

The results of our calculations are based on a Monte Carlo integration of the three-body phase space, including the mentioned elementary reaction amplitudes for $KN$ and $\pi N \to K\Lambda$, that involves $10^6$ sample events. To determine resonance parameters from the Dalitz plot and the $K\Lambda$ helicity angle spectra it is necessary to accumulate a data set with large statistics. Only then it is possible to achieve an acceptable confidence level for the extracted resonance and ($\Lambda p$) effective-range parameters. In this context we would like to point out that presently the estimates [79] for the mass and width of the $S_{11}(1650)$-resonance are rather uncertain: $1640 \le M_R \le 1680\,\mathrm{MeV}$ and $145 \le \Gamma_R \le 190\,\mathrm{MeV}$, respectively. The quoted $P_{11}(1710)$-resonance parameters are $1680 \le M_R \le 1740\,\mathrm{MeV}$ for the mass and $50 \le \Gamma_R \le 250\,\mathrm{MeV}$ for width. The uncertainties of the decay rates of the resonances to the $K\Lambda$ mode is 3–11% and 5–25% for the $S_{11}$ and $P_{11}$, respectively.

We would like to thank W. Eyrich, C. Hanhart, E. Kuhlmann, U.-G. Meißner, J. Niskanen, J. Ritman, E. Roderburg, S. Schadmand and W. Schroeder for useful discussions. This work was partially supported by the Deutsche Forschungsgemeinschaft through funds provided to the SFB/TR 16 "Subnuclear Structure of Matter". This research is part of the EU Integrated Infrastructure Initiative Hadron Physics Project under contract number RII3-CT-2004-506078. A.S. acknowledges support by the COSY FFE grant No. 41760632 (COSY-085).

## References

1. E. Ferrari, Nuovo Cimento **15**, 652 (1960).
2. T. Yao, Phys. Rev. **125**, 1048 (1962).
3. J.Q. Wu, C.M. Ko, Nucl. Phys. A **499**, 810 (1989).
4. J.M. Laget, Phys. Lett. B **259**, 24 (1991).
5. A. Deloff, Nucl. Phys. A **505**, 583 (1989).
6. A. Sibirtsev, Phys. Lett. B **359**, 29 (1995).
7. G. Bunce *et al.*, Phys. Rev. Lett. **36**, 1113 (1976).
8. L.G. Pondrom, Phys. Rep. **122**, 57 (1985).
9. B. Lundberg *et al.*, Phys. Rev. D **40**, 3557 (1989).
10. A.M. Smith *et al.*, Phys. Lett. B **185**, 209 (1987).
11. J. Soffer, N.A. Törnqvist, Phys. Rev. Lett. **68**, 907 (1992).
12. A.V. Turbiner, JETP Lett. **22**, 182 (1975).
13. A.V. Turbiner, Sov. J. Nucl. Phys. **22**, 551 (1976).
14. A.A. Sibirtsev, Sov. J. Nucl. Phys. **55**, 145 (1992).
15. J.T. Balewski *et al.*, Phys. Lett. B **388**, 859 (1996).
16. J.T. Balewski *et al.*, Phys. Lett. B **420**, 211 (1998).
17. S. Sewerin *et al.*, Phys. Rev. Lett. **83**, 682 (1999) [arXiv:nucl-ex/9811004].
18. P. Moskal *et al.*, J. Phys. G **28**, 1777 (2002) [arXiv:nucl-ex/0201016].
19. M. Wolke *et al.*, Nucl. Phys. A **721**, 683 (2003) [arXiv:nucl-ex/0302013].
20. P. Kowina *et al.*, Eur. Phys. J. A **18**, 351 (2003) [arXiv:nucl-ex/0302014].
21. P. Kowina *et al.*, Eur. Phys. J. A **22**, 293 (2004) [arXiv:nucl-ex/0402008].
22. T. Rozek *et al.*, Int. J. Mod. Phys. A **20**, 680 (2005) [arXiv:nucl-ex/0407024].
23. H. Brand *et al.*, Phys. Lett. B **420**, 217 (1998).
24. K. Tsushima, A. Sibirtsev, A.W. Thomas, Phys. Lett. B **390**, 29 (1997) [arXiv:nucl-th/9608029].
25. A. Sibirtsev, K. Tsushima, A.W. Thomas, Phys. Lett. B **421**, 59 (1998) [arXiv:nucl-th/9711028].
26. K. Tsushima, A. Sibirtsev, A.W. Thomas, Phys. Rev. C **59**, 369 (1999) [arXiv:nucl-th/9801063].
27. G. Fäldt, C. Wilkin, Z. Phys. A **357**, 241 (1997) [arXiv:nucl-th/9612019].
28. A. Sibirtsev, K. Tsushima, W. Cassing, A.W. Thomas, arXiv:nucl-th/0004022.

29. R. Shyam, G. Penner, U. Mosel, Phys. Rev. C **63**, 022202 (2001) [arXiv:nucl-th/0010102].
30. R. Shyam, Phys. Rev. C **60**, 055213 (1999) [arXiv:nucl-th/9901038].
31. J.T. Balewski *et al.*, Eur. Phys. J. A **2**, 99 (1998) [arXiv:nucl-ex/9803008].
32. P. Moskal, M. Wolke, A. Khoukaz, W. Oelert, Prog. Part. Nucl. Phys. **49**, 1 (2002) [arXiv:hep-ph/0208002].
33. F. Hinterberger, A. Sibirtsev, Eur. Phys. J. A **21**, 313 (2004) [arXiv:nucl-ex/0402021].
34. A. Gasparyan, J. Haidenbauer, C. Hanhart, J. Speth, Phys. Rev. C **69**, 034006 (2004) [arXiv:hep-ph/0311116].
35. C. Hanhart, Phys. Rep. **397**, 155 (2004) [arXiv:hep-ph/0311341].
36. A. Gasparyan, J. Haidenbauer, C. Hanhart, Phys. Rev. C **72**, 034006 (2005) [arXiv:nucl-th/0506067].
37. B. Holzenkamp *et al.*, Nucl. Phys. A **500**, 485 (1989).
38. A. Reuber, K. Holinde, J. Speth, Nucl. Phys. A **570**, 543 (1994).
39. Th. A. Rijken, V.G.J. Stoks, Y. Yamamoto, Phys. Rev. C **59**, 21 (1999).
40. J. Haidenbauer, U.-G. Meißner, Phys. Rev. C **72**, 044005 (2005) [arXiv:nucl-th/0506019].
41. E. Byckling, K. Kajantie, *Particle Kinematics* (John Willey and Sons Publ., 1972).
42. R.H. Dalitz, Philos. Mag. **44**, 1068 (1953).
43. K. Gottfried, J.D. Jackson, Nuovo Cimento **33**, 309 (1964).
44. J.D. Jackson, Nuovo Cimento **34**, 1 (1964).
45. S.B. Treiman, C.N. Yang, Phys. Rev. Lett. **8**, 140 (1962).
46. W. Koch, *Analysis of Scattering and Decay* (Gordon and Breach Publ., 1968).
47. G. Höhler, *Elastic and Charge Exchange Scattering of Elementary Particles*, Landolt-Börnstein, New Ser. **9**, 492 (1983).
48. A. Sibirtsev, W. Cassing, arXiv:nucl-th/9802019.
49. A. Gasparian, J. Haidenbauer, C. Hanhart, L. Kondratyk, J. Speth, Phys. Lett. B **480**, 273 (2000) [arXiv:nucl-th/9909017].
50. R. Büttgen, K. Holinde, A. Müller-Groeling, J. Speth, P. Wyborny, Nucl. Phys. A **506**, 586 (1990).
51. M. Hoffmann, J.W. Durso, K. Holinde, B.C. Pearce, J. Speth, Nucl. Phys. A **593**, 341 (1995).
52. J. Haidenbauer, G. Krein, Phys. Rev. C **68**, 052201 (2003) [arXiv:hep-ph/0309243].
53. A. Sibirtsev, J. Haidenbauer, S. Krewald, Ulf-G. Meißner, Phys. Lett. B **599**, 230 (2004) [arXiv:hep-ph/0405099].
54. V.V. Barmin *et al.*, Phys. At. Nucl. **66**, 1715 (2003); Yad. Fiz. **66**, 1763 (2003) [arXiv:hep-ex/0304040].
55. A. Sibirtsev, J. Haidenbauer, S. Krewald, Ulf-G. Meißner, Eur. Phys. J. A **23**, 491 (2005).
56. V.B. Berestetsky, I.Ya. Pomeranchuk, Nucl. Phys. **22**, 629 (1961).
57. E. Ferrari, F. Selleri, Suppl. Nuovo Cimento **26**, 451 (1962).
58. A.A. Sibirtsev, Nucl. Phys. A **604**, 455 (1996).
59. A. Sibirtsev, W. Cassing, C.M. Ko, Z. Phys. A **358**, 101 (1997) [arXiv:nucl-th/9612040].
60. A. Gasparyan, J. Haidenbauer, C. Hanhart, J. Speth, Phys. Rev. C **68**, 045207 (2003) [arXiv:nucl-th/0307072].
61. M. Sotona, J. Zofka, Prog. Theor. Phys. **81**, 160 (1989).
62. A. Krzywicki, J. Tran Thanh Van, Phys. Lett. B **30**, 185 (1969).
63. A.C. Irving, A.D. Martin, C. Michael, Nucl. Phys. B **32**, 1 (1971).
64. B.J. Hartley, G.L. Kane, Nucl. Phys. B **57**, 157 (1973).
65. A.C. Irving, R.P. Worden, Phys. Rep. C **34**, 119 (1977).
66. A.C. Irving *et al.*, Nucl. Phys. B **32**, 1 (1971).
67. A. Baldini, V. Flamino, W.G. Moorhead, D.R.O. Morrison, Landolt-Börnstein, New Ser. **12** (1988).
68. T.M. Knasel *et al.*, Phys. Rev. D **11**, 1 (1975).
69. R.D. Baker *et al.*, Nucl. Phys. B **141**, 29 (1978).
70. M.L. Goldberger, K.M. Watson, *Collision Theory* (John Willey and Sons, 1967).
71. A. Sibirtsev, S. Schneider, C. Elster, J. Haidenbauer, S. Krewald, J. Speth, Phys. Rev. C **65**, 044007 (2002) [arXiv:nucl-th/0111086].
72. A. Sibirtsev, S. Schneider, C. Elster, J. Haidenbauer, S. Krewald, J. Speth, Phys. Rev. C **65**, 067002 (2002) [arXiv:nucl-th/0203039].
73. A. Sibirtsev, C. Elster, J. Haidenbauer, J. Speth, Phys. Rev. C **64**, 024006 (2001) [arXiv:nucl-th/0104011].
74. A. Sibirtsev, J. Haidenbauer, S. Krewald, U.-G. Meißner, Phys. Rev. D **71**, 054010 (2005) [arXiv:nucl-th/0203039].
75. K.M. Watson, Phys. Rev. **88**, 1163 (1952).
76. A.B. Migdal, Sov. Phys. JETP **1**, 2 (1955).
77. D.H. Saxon *et al.*, Nucl. Phys B **162**, 522 (1980).
78. K.W. Bell *et al.*, Nucl. Phys. B **222**, 389 (1983).
79. S. Eidelman *et al.*, Phys. Lett. B **592**, 1 (2004).